

# Analysis of old very metal rich stars in the solar neighbourhood $\star$ , $\star\star$

M. Trevisan<sup>1</sup>, B. Barbuy<sup>1</sup>, K. Eriksson<sup>2</sup>, B. Gustafsson<sup>2</sup>, M. Grenon<sup>3</sup>, and L. Pompéia<sup>4</sup>

<sup>1</sup> Universidade de São Paulo, Rua do Matão 1226, São Paulo 05508-900, Brazil  
e-mail: trevisan@astro.iag.usp.br, barbuy@astro.iag.usp.br

<sup>2</sup> Department of Astronomy and Space Physics, Uppsala University, Box 515, SE 751 20 Uppsala, Sweden  
e-mail: kjell.eriksson@fysast.uu.se, bengt.gustafsson@astro.uu.se

<sup>3</sup> Observatoire de Genève, 51 Chemin des Maillettes, 1290 Sauverny, Switzerland  
e-mail: michel.grenon@unige.ch

<sup>4</sup> Universidade do Vale do Paraíba, Av. Shishima Hifumi 2911, São José dos Campos, 12244-000 São Paulo, Brazil  
e-mail: pompeia@univap.br

Accepted for publication in Astronomy & Astrophysics, 2011 September 8

## ABSTRACT

**Context.** A sample of mostly old metal-rich dwarf and turn-off stars with high eccentricity and low maximum height above the Galactic plane has been identified. From their kinematics, it was suggested that the inner disk is their most probable birthplace. Their chemical imprints may therefore reveal important information about the formation and evolution of the still poorly understood inner disk.

**Aims.** To probe the formation history of these stellar populations, a detailed analysis of a sample of very metal-rich stars is carried out. We derive the metallicities, abundances of  $\alpha$  elements, ages, and Galactic orbits.

**Methods.** The analysis of 71 metal-rich stars is based on optical high-resolution échelle spectra obtained with the FEROS spectrograph at the ESO 1.52-m Telescope at La Silla, Chile. The metallicities and abundances of C, O, Mg, Si, Ca, and Ti were derived based on LTE detailed analysis, employing the MARCS model atmospheres.

**Results.** We confirm the high metallicity of these stars reaching up to  $[\text{Fe}/\text{H}] = 0.58$ , and the sample of metal-rich dwarfs can be kinematically subclassified in samples of thick disk, thin disk, and intermediate stellar populations. All sample stars show solar  $\alpha$ -Fe ratios, and most of them are old and still quite metal rich. The orbits suggest that the thin disk, thick disk and intermediate populations were formed at Galactocentric distances of  $\sim 8$  kpc,  $\sim 6$  kpc, and  $\sim 7$  kpc, respectively. The mean maximum height of the thick disk subsample of  $Z_{\text{max}} \sim 380$  pc, is lower than for typical thick disk stars. A comparison of  $\alpha$ -element abundances of the sample stars with bulge stars shows that the oxygen is compatible with a bulge or inner thick disk origin. Our results suggest that models of radial mixing and dynamical effects of the bar and bar/spiral arms might explain the presence of these old metal-rich dwarf stars in the solar neighbourhood.

**Key words.** stars: abundances, atmospheres, late-type, – Galaxy: solar neighbourhood.

## 1. Introduction

The formation and properties of the thin and thick disks of our Galaxy have been the subject of several studies, and several scenarios have been proposed to explain their formation (e.g. Schönrich & Binney 2009a,b; Villalobos et al. 2010, and references therein). In each scenario, typical signatures into the velocity and metallicity distribution of stars are imprinted. For this reason there have been numerous studies devoted to determination of the thick disk velocity ellipsoid and metallicity distribution, the study of the thin disk to the thick disk interface, abundance trends and correlations between abundance and kinematics, or the existence of gradients (e.g. Ivezić et al. 2008; Katz et al. 2011).

It is well-known that thick disk stars move on higher eccentricity orbits and present larger velocity dispersions than thin

disk stars. The thick disk is a more slowly rotating stellar system than the thin disk, and as a whole it lags behind the local standard of rest by  $\sim 50$  km s<sup>-1</sup>, while the thin disk component lags by only  $\sim 12$  km s<sup>-1</sup> (Soubiran et al. 2003; Robin et al. 2003). Thick disk stars also appear to be significantly older than thin disk ones (Fuhrmann 1998).

On the other hand, the behaviour of the chemical abundance characteristics of these components still is a matter of debate. Some studies suggest that the thick disk component is composed mainly of metal-poor stars (e.g. Chiba & Beers 2000; Reddy & Lambert 2008), while metal-rich stars appear to be restricted to the thin disk, with a transition occurring at  $[\text{Fe}/\text{H}] \sim -0.3$  (Mishenina et al. 2004; Reddy et al. 2006). Previous results show that thick disk stars exhibit a larger abundance of  $\alpha$ -elements relative to iron than the thin disk members (Fuhrmann 1998; Gratton et al. 2000; Ruchti et al. 2010). Bensby et al. (2003) and Feltzing et al. (2003) found that thick disk stars extend to solar metallicities, showing an inflexion in  $[\alpha/\text{Fe}]$  vs.  $[\text{Fe}/\text{H}]$  around  $[\text{Fe}/\text{H}] \sim -0.5$ , reaching the solar ratios at  $[\text{Fe}/\text{H}] \sim 0.0$ . Also, a new population has been identified in several studies: Reddy et al. (2006) and Haywood (2008) identify a population having thick disk kinematics but thin disk

Send offprint requests to: M. Trevisan

\* Observations collected at the European Southern Observatory, La Silla, Chile

\*\* Tables A.1 to A.4 are only available in electronic form at the CDS via anonymous ftp to cdsarc.u-strasbg.fr (130.79.128.5) or via http://cdsweb.u-strasbg.fr/cgi-bin/qcat?J/A+A/

abundances (TKTA subsample in Reddy et al.). Mishenina et al. (2004) and Soubiran & Girard (2005) find metal-rich stars with kinematics of the thick disk.

A detailed study of stars with these properties can clarify the origin of this population. Therefore, in this work we study a sample of 71 metal-rich stars in terms of kinematics and abundances.

The paper is organized as follows. In Sect. 2, a description of the sample is presented, and the observations and reductions are described in Sect. 3. The Galactic orbits are derived in Sect. 4. Derivations of stellar parameters effective temperatures, gravities, and metallicities are given in Sect. 5. In Sect. 6, the element abundances are derived. In Sect. 7 the present results are compared with other samples from the literature, and we briefly discuss the possible origins of the identified stellar populations in the context of the Galaxy formation. Finally, results are summarized in Sect. 8.

## 2. Sample selection

Grenon (1972, 1989, 1990, 1998, 2000) selected 7824 high proper motion stars from the New Luyten's Two Tenths catalogue (NLTT) (a catalogue of nearby stars with proper motions  $\mu > 0.18 \pm 0.02$  arcsec yr<sup>-1</sup>) that have been included in the HIPPARCOS programme. Among these, radial velocities and Geneva photometry were gathered for 5443 stars. Only stars with parallaxes larger than 10 mas were kept for the study presented in Raboud et al. (1998). Among these, space velocities were measured for 4143 stars, and metallicities from Geneva photometry were gathered for 2619 of them. From their kinematics, Raboud et al. (1998) found that the old disk stars in this sample appeared to show a positive mean U motion. In particular, an imbalance between positive and negative U velocities was found for old disk stars selected in the parallax range 10 to 40 mas (with U positive in the direction of the anti-centre), reaching up to 50 km s<sup>-1</sup>. After corrections for local motions, the U anomaly is  $+29 \pm 2$  km s<sup>-1</sup> with respect to the Sun, and  $+19 \pm 9$  km s<sup>-1</sup> with respect to the Galactic centre. Raboud et al. suggested that the metal-rich stars within this sample appear to wander from inside the bar, reaching the solar neighbourhood.

A subsample of 202 of these stars was selected for this project by M. Grenon when gathering the oldest disk stars, with high metallicities and eccentricities, as well as thin disk very metal-rich stars. We were able to obtain high-resolution spectra for 100 of them using the FEROS spectrograph at the 1.5m ESO telescope at La Silla, during an IAG/ON and ON/ESO agreement in 1999-2002.

The Geneva photometry was used by Grenon (1978) to derive the effective temperatures, absolute magnitudes, and metallicities, with internal errors of 20–40 K on effective temperature  $T_{\text{eff}}$ , 0.03 – 0.05 dex on metallicity [M/H] and 0.15 on V magnitudes.

For the present analysis, we selected the 71 most metal-rich stars of the sample of 100 observed stars, indicated by Geneva photometry to have [Fe/H] > 0.00, hereafter called *sample stars*. A study of  $\alpha$ -elements vs. [Fe/H] in their full metallicity range, for 36 among the 100 observed such stars, covering  $-0.8 < [\text{Fe}/\text{H}] < +0.4$ , was presented by Pompéia et al. (2003). There are 12 stars in common between the present sample and Pompéia et al. (2003), where another 24 stars with metallicities below solar, were also analysed, with the aim of identifying the downturn knee of  $[\alpha/\text{Fe}]$  vs. [Fe/H], as discussed in Sect. 7. All the stars in the sample have parallaxes larger than 10 mas, with errors of 6% in average.

Table A.1 shows the log of spectroscopic observations (available electronically only).

## 3. Observations and reductions

Optical spectra were obtained using the Fiber Fed Extended Range Optical Spectrograph (FEROS) (Kaufer et al. 2000) at the 1.52 m telescope at ESO, La Silla. The total wavelength coverage is 3560-9200 Å with a resolving power of  $(R = \lambda/\Delta\lambda) = 48,000$ . Two fibres, with entrance aperture of 2.7 arcsec, simultaneously recorded star light and sky background. The detector is a back-illuminated CCD with 2948 x 4096 pixels of 15 μm size.

Reductions were carried out through a pipeline package for reductions (DRS) of FEROS data, in MIDAS environment. The pipeline performs the subtraction of bias and scattered light in the CCD, orders extraction, flatfielding and wavelength calibration with a ThAr calibration frame. The data reduction proceeded in the IRAF environment as follows. The spectra were cut into parts of 500 Å each using the SCOPY task, and the normalization was carried out with the CONTINUUM task. Spectra of rapidly rotating hot B stars at similar airmasses as the target were also observed, in order to correct for telluric lines using the TELLURIC task. The radial and heliocentric velocities,  $v_r$  and  $v_{\text{HeliO}}$ , were determined using the RVCORRECT task. The standard errors of the velocities are  $\sim 0.2$  km s<sup>-1</sup>. Typical signal-to-noise ratios of the spectra were obtained considering average values at different wavelengths. The mean signal-to-noise ratio for the sample stars is  $\sim 100$ , as reported in Table A.1.

## 4. Kinematics

Grenon (1999) found that the high metallicity stars in the sample have low maximum height from the Galactic plane  $Z_{\text{max}}$ , and their turn-off location indicated an age of  $\sim 10$  Gyr. The identification of an old population with such a high metallicity and low  $Z_{\text{max}}$  is unexpected. In order to investigate the kinematical properties of the sample stars, we derive the Galactic orbits in Sect. 4.1, using the GRINTON integrator (Carraro et al. 2002; Bedin et al. 2006). In Sect. 4.2, we separate the sample into thin disk and thick disk stars, based on kinematical criteria. We assigned a probability of each star belonging to either the thin or the thick disk, assuming that the space velocities of each population follow a Gaussian distribution as defined by Soubiran et al. (2003).

### 4.1. Galactic orbits

Grenon (1999) derived U, V, W space velocities for all the sample stars. U, V, W are defined in a right-handed Galactic system with U pointing outwards the Galactic centre, V in the direction of rotation and W towards the north Galactic pole. We used the GRINTON integrator to calculate the Galactic orbits, with these velocities and the HIPPARCOS parallaxes. This code integrates the orbits back in time for several Galactic revolutions and returns the minimum and maximum distances from the Galactic centre ( $R_{\text{min}}$ ,  $R_{\text{max}}$ ), maximum height from the Galactic plane ( $Z_{\text{max}}$ ) and the eccentricity  $e$  of the orbit. Before using the observed space motions, these were transformed to the local standard of rest. We used a solar motion of (-10.0, 5.3, 7.2) km s<sup>-1</sup> (Dehnen & Binney 1998). The gravitational potential used in the orbit integration is a simple one (Allen & Santillan 1991), for which a circular rotation speed of 220 km s<sup>-1</sup> and a disk volume

Table 1: Basic stellar data

Star	$T_{\text{Gen}}$ (K)	V	J	$K_S$	$M_{\text{BoI}}$	$BC_V$	$\pi$ (mas)	d (pc)
G 161-029	4869	10.33	$9.52 \pm 0.02$	$8.90 \pm 0.02$	...	-0.41	...	...
BD-02 180	4917	10.09	$8.44 \pm 0.02$	$7.89 \pm 0.02$	5.59	-0.29	$14.41 \pm 1.62$	$69 \pm 8$
BD-05 5798	4875	10.38	$8.64 \pm 0.03$	$8.07 \pm 0.04$	5.68	-0.35	$13.48 \pm 1.94$	$74 \pm 11$
BD-17 6035	4830	10.30	$8.53 \pm 0.03$	$7.98 \pm 0.02$	5.71	-0.35	$14.23 \pm 2.41$	$70 \pm 12$
CD-32 0327	5001	10.41	$8.75 \pm 0.03$	$8.16 \pm 0.03$	5.88	-0.32	$14.41 \pm 1.77$	$69 \pm 9$
CD-40 15036	5341	10.08	$8.69 \pm 0.02$	$8.27 \pm 0.02$	5.08	-0.16	$10.75 \pm 1.70$	$93 \pm 15$
HD 8389	5135	7.85	$6.39 \pm 0.02$	$5.92 \pm 0.02$	5.27	-0.18	$33.09 \pm 0.99$	$30 \pm 1$
HD 9174	5459	8.40	$7.13 \pm 0.02$	$6.74 \pm 0.03$	4.03	-0.10	$14.04 \pm 1.13$	$71 \pm 6$
HD 9424	5332	9.17	$7.81 \pm 0.03$	$7.38 \pm 0.02$	5.17	-0.15	$16.94 \pm 0.99$	$59 \pm 3$
HD 10576	5883	8.51	$7.41 \pm 0.03$	$7.07 \pm 0.03$	3.77	-0.08	$11.66 \pm 0.73$	$86 \pm 5$
HD 11608	4917	9.31	$7.61 \pm 0.02$	$7.07 \pm 0.03$	5.91	-0.31	$24.12 \pm 1.34$	$41 \pm 2$
HD 12789	5706	8.89	$7.74 \pm 0.02$	$7.38 \pm 0.02$	4.00	-0.08	$10.92 \pm 1.00$	$92 \pm 8$
HD 13386	5131	8.91	$7.39 \pm 0.02$	$6.97 \pm 0.02$	5.46	-0.19	$22.27 \pm 1.09$	$45 \pm 2$
HD 15133	5113	9.36	$7.85 \pm 0.03$	$7.38 \pm 0.02$	5.33	-0.20	$17.18 \pm 1.38$	$58 \pm 5$
HD 15555	4793	7.34	$5.60 \pm 0.02$	$4.99 \pm 0.02$	3.42	-0.37	$19.45 \pm 1.06$	$51 \pm 3$
HD 16905	4821	9.44	$7.65 \pm 0.02$	$7.09 \pm 0.02$	6.06	-0.37	$24.94 \pm 0.93$	$40 \pm 1$
HD 25061	5247	9.27	$7.84 \pm 0.02$	$7.36 \pm 0.02$	5.35	-0.18	$17.86 \pm 0.82$	$56 \pm 3$
HD 26151	5285	8.49	$7.08 \pm 0.02$	$6.65 \pm 0.03$	5.02	-0.16	$21.79 \pm 1.12$	$46 \pm 2$
HD 26794	4932	8.78	$7.07 \pm 0.02$	$6.49 \pm 0.02$	5.83	-0.34	$30.02 \pm 1.68$	$33 \pm 2$
HD 27894	4879	9.36	$7.64 \pm 0.02$	$7.07 \pm 0.03$	5.89	-0.34	$23.60 \pm 0.91$	$42 \pm 2$
HD 30295	5350	8.86	$7.49 \pm 0.02$	$7.04 \pm 0.02$	4.88	-0.15	$17.14 \pm 0.77$	$58 \pm 3$
HD 31452	5206	8.43	$6.94 \pm 0.03$	$6.47 \pm 0.02$	5.26	-0.20	$25.50 \pm 1.27$	$39 \pm 2$
HD 31827	5463	8.26	$7.00 \pm 0.02$	$6.61 \pm 0.02$	4.56	-0.10	$19.05 \pm 0.69$	$52 \pm 2$
HD 35854	4943	7.70	$6.01 \pm 0.03$	$5.39 \pm 0.02$	6.08	-0.35	$55.76 \pm 0.76$	$18 \pm 0$
HD 37986	5455	7.36	$6.06 \pm 0.02$	$5.62 \pm 0.02$	5.02	-0.13	$36.05 \pm 0.92$	$28 \pm 1$
HD 39213	5337	8.96	$7.61 \pm 0.02$	$7.20 \pm 0.02$	4.82	-0.13	$15.75 \pm 0.91$	$63 \pm 4$
HD 39715	4781	8.84	$6.99 \pm 0.03$	$6.35 \pm 0.02$	6.28	-0.44	$37.57 \pm 1.26$	$27 \pm 1$
HD 43848	5091	8.65	$7.12 \pm 0.03$	$6.61 \pm 0.02$	5.58	-0.22	$26.99 \pm 0.83$	$37 \pm 1$
HD 77338	5283	8.63	$7.22 \pm 0.02$	$6.76 \pm 0.02$	5.39	-0.16	$24.23 \pm 1.18$	$41 \pm 2$
HD 81767	4943	9.45	$7.77 \pm 0.02$	$7.21 \pm 0.02$	5.74	-0.31	$20.89 \pm 1.49$	$48 \pm 3$
HD 82943	5849	6.54	$5.51 \pm 0.02$	$5.11 \pm 0.02$	4.28	-0.07	$36.42 \pm 0.84$	$27 \pm 1$
HD 86065	4963	9.36	$7.65 \pm 0.03$	$7.09 \pm 0.02$	6.14	-0.33	$26.42 \pm 1.25$	$38 \pm 2$
HD 86249	4935	8.99	$7.32 \pm 0.02$	$6.74 \pm 0.02$	6.02	-0.32	$29.57 \pm 1.16$	$34 \pm 1$
HD 87007	5302	8.82	$7.35 \pm 0.02$	$6.89 \pm 0.04$	5.46	-0.19	$23.23 \pm 1.41$	$43 \pm 3$
HD 90054	5986	7.87	$6.85 \pm 0.02$	$6.52 \pm 0.02$	3.63	-0.05	$14.52 \pm 0.97$	$69 \pm 5$
HD 91585	5077	9.43	$7.90 \pm 0.03$	$7.37 \pm 0.03$	5.66	-0.24	$19.67 \pm 1.33$	$51 \pm 3$
HD 91669	5175	9.70	$8.26 \pm 0.02$	$7.77 \pm 0.02$	4.95	-0.18	$12.19 \pm 1.52$	$82 \pm 10$
HD 93800	5129	9.12	$7.58 \pm 0.02$	$7.10 \pm 0.02$	5.32	-0.22	$19.18 \pm 1.42$	$52 \pm 4$
HD 94374	4825	9.27	$7.42 \pm 0.02$	$6.79 \pm 0.02$	6.13	-0.43	$28.70 \pm 1.29$	$35 \pm 2$
HD 95338	5144	8.62	$7.10 \pm 0.02$	$6.59 \pm 0.02$	5.56	-0.23	$27.14 \pm 0.91$	$37 \pm 1$
HD 104212	5694	8.38	$7.24 \pm 0.02$	$6.88 \pm 0.03$	3.62	-0.08	$11.59 \pm 1.09$	$86 \pm 8$
HD 107509	5944	7.91	$6.90 \pm 0.02$	$6.58 \pm 0.03$	3.68	-0.06	$14.65 \pm 0.82$	$68 \pm 4$
HD 120329	5511	8.34	$7.09 \pm 0.02$	$6.69 \pm 0.02$	4.00	-0.11	$14.24 \pm 1.05$	$70 \pm 5$
HD 143102	5432	7.88	$6.59 \pm 0.02$	$6.17 \pm 0.02$	3.51	-0.12	$14.13 \pm 0.99$	$71 \pm 5$
HD 148530	5346	8.81	$7.42 \pm 0.03$	$6.97 \pm 0.02$	5.31	-0.17	$21.50 \pm 1.27$	$47 \pm 3$
HD 149256	5271	8.42	$7.04 \pm 0.02$	$6.60 \pm 0.02$	3.89	-0.15	$13.32 \pm 1.21$	$75 \pm 7$
HD 149606	4936	8.95	$7.25 \pm 0.02$	$6.72 \pm 0.02$	6.09	-0.31	$30.89 \pm 1.37$	$32 \pm 1$
HD 149933	5424	8.05	$6.72 \pm 0.02$	$6.29 \pm 0.03$	5.03	-0.14	$26.56 \pm 1.22$	$38 \pm 2$
HD 165920	5261	7.91	$6.50 \pm 0.03$	$6.03 \pm 0.02$	5.22	-0.17	$31.27 \pm 1.12$	$32 \pm 1$
HD 168714	5552	8.90	$7.67 \pm 0.02$	$7.31 \pm 0.02$	4.33	-0.09	$12.67 \pm 1.51$	$79 \pm 9$
HD 171999	5257	8.34	$6.89 \pm 0.02$	$6.43 \pm 0.02$	5.31	-0.18	$26.97 \pm 1.12$	$37 \pm 2$
HD 177374	5011	9.40	$7.75 \pm 0.03$	$7.24 \pm 0.02$	5.44	-0.28	$18.35 \pm 1.65$	$54 \pm 5$
HD 179764	5374	9.01	$7.58 \pm 0.02$	$7.11 \pm 0.02$	4.84	-0.19	$15.98 \pm 1.30$	$63 \pm 5$
HD 180865	5132	8.97	$7.45 \pm 0.02$	$6.98 \pm 0.02$	5.54	-0.21	$22.66 \pm 1.32$	$44 \pm 3$
HD 181234	5220	8.59	$7.15 \pm 0.03$	$6.69 \pm 0.02$	4.97	-0.17	$20.49 \pm 1.19$	$49 \pm 3$
HD 181433	4866	8.40	$6.66 \pm 0.02$	$6.09 \pm 0.02$	5.97	-0.35	$38.24 \pm 1.15$	$26 \pm 1$
HD 182572	5461	5.17	$3.55 \pm 0.21$	$3.04 \pm 0.32$	4.01	-0.26	$66.01 \pm 0.77$	$15 \pm 1$
HD 196397	5267	8.95	$7.59 \pm 0.02$	$7.13 \pm 0.03$	5.20	-0.15	$19.01 \pm 1.65$	$53 \pm 5$
HD 196794	5075	8.52	$6.94 \pm 0.03$	$6.41 \pm 0.02$	5.99	-0.26	$35.22 \pm 1.14$	$28 \pm 1$
HD 197921	4866	9.25	$7.49 \pm 0.02$	$6.90 \pm 0.02$	5.82	-0.37	$24.45 \pm 1.58$	$41 \pm 3$
HD 201237	4886	10.10	$8.31 \pm 0.02$	$7.71 \pm 0.02$	4.97	-0.39	$11.23 \pm 2.09$	$89 \pm 17$
HD 209721	5388	9.51	$8.18 \pm 0.02$	$7.77 \pm 0.02$	4.59	-0.13	$11.00 \pm 1.26$	$91 \pm 10$
HD 211706	5830	8.90	$7.84 \pm 0.02$	$7.52 \pm 0.02$	4.19	-0.07	$11.78 \pm 1.40$	$85 \pm 10$
HD 213996	5203	8.66	$7.21 \pm 0.03$	$6.76 \pm 0.03$	5.30	-0.18	$23.10 \pm 1.14$	$43 \pm 2$
HD 214463	4958	9.67	$8.10 \pm 0.02$	$7.59 \pm 0.02$	5.29	-0.24	$14.90 \pm 1.77$	$67 \pm 8$
HD 218566	4834	8.59	$6.82 \pm 0.02$	$6.22 \pm 0.02$	5.83	-0.38	$33.40 \pm 1.19$	$30 \pm 1$
HD 218750	5122	9.25	$7.71 \pm 0.02$	$7.18 \pm 0.03$	5.34	-0.24	$18.45 \pm 1.50$	$54 \pm 4$
HD 221313	5075	9.90	$8.38 \pm 0.02$	$7.85 \pm 0.02$	5.16	-0.23	$12.52 \pm 1.79$	$80 \pm 11$
HD 221974	5109	9.31	$7.80 \pm 0.02$	$7.32 \pm 0.02$	5.68	-0.20	$20.61 \pm 1.53$	$49 \pm 4$
HD 224230	4900	9.97	$8.24 \pm 0.03$	$7.63 \pm 0.03$	6.16	-0.36	$20.43 \pm 1.22$	$49 \pm 3$
HD 224383	5689	7.89	$6.74 \pm 0.03$	$6.33 \pm 0.02$	4.40	-0.10	$20.98 \pm 1.24$	$48 \pm 3$

density of  $0.15M_{\odot} \text{ pc}^{-3}$  are adopted and a solar Galactocentric distance  $R_{\odot} = 8.5 \text{ kpc}$  is assumed.

Uncertainties in the orbital parameters were obtained using the bootstrapping technique, as follows. We integrated the orbit of each star 500 times. At each integration, the input parameters, U, V, W velocities and the parallax  $\pi$ , were varied following a normal distribution with mean  $X$  and standard deviation

of  $\sigma_X$ , where  $X$  is the parameter value and  $\sigma_X$  the error associated with it. The final orbital parameters  $R_{\text{min}}$ ,  $R_{\text{max}}$ ,  $Z_{\text{max}}$ , and eccentricity, and their errors were then computed as the mean and standard deviation of the output values of these 500 realizations. Uncertainties in  $R_{\text{min}}$ ,  $R_{\text{max}}$ , and  $Z_{\text{max}}$  are typically  $\approx 0.30 \text{ kpc}$ ,  $0.60 \text{ kpc}$ , and  $0.05 \text{ kpc}$ , respectively. The derived orbital parameters are listed in Table 12. Our sample contains 17 stars in



common with the Geneva-Copenhagen survey (Holmberg et al. 2009), hereafter referred to as GCS, as listed in Table 2. We compared the orbital parameters derived here with the values from the GCS survey. We found that our  $R_{\min}$  distances are  $\sim 6\%$  lower and  $R_{\max}$  are  $\sim 5\%$  higher on average. For the orbit eccentricities, we derived values which are  $\sim 16\%$  higher than eccentricities from GCS. The maximum height from the Galactic plane from GCS are  $\sim 80$  pc lower ( $\sim 30\%$ ) than our sample, on average.

It is important to stress that the gravitational potential used in the orbit integration does not take the Galactic bar into account. The bar potential could affect the orbits of our stars, since  $R_{\min}$  are as close as 3-4 kpc from the Galactic centre.

#### 4.2. Thin and thick disk membership probabilities

Identifying stellar populations in velocity space is not straightforward. Thus, before discussing whether the sample stars belong to the thin or thick disk, we must analyse the criteria used to define the membership probabilities.

The separation between thin and thick disks can be done either by selecting stars based on their kinematics, using chemical composition criteria, or a combination of both. Usually, separation based only on kinematics or abundances are not equivalent: thick (thin) disk samples selected on kinematical criteria can contain stars with thin (thick) chemical abundances (e.g. Mishenina et al. 2004; Reddy et al. 2006). Some authors argue that, since the chemical composition of a star does not change with time, while kinematics may change, the selection based on abundances is more reliable. On the other hand, if we want to trace the formation of the disk components through the study of the chemical abundances of their stars, the abundances must not be used to define these components. Therefore, here we assign the probability of each star belonging to either the thin disk or the thick disk by adopting the kinematical approach used in previous studies by Bensby et al. (2004), Mishenina et al. (2004), and Reddy et al. (2006). The procedure relies on the assumption that the space velocities of each population follow a Gaussian distribution, with given mean values and dispersions  $\sigma_U$ ,  $\sigma_V$ ,  $\sigma_W$ . The equations determining the probabilities are

$$p_{\text{thin}} = f_1 \frac{p_1}{p}, \quad p_{\text{thick}} = f_2 \frac{p_2}{p}, \quad p_{\text{halo}} = f_3 \frac{p_3}{p} \quad (1)$$

where  $p_{\text{thin}}$ ,  $p_{\text{thick}}$ ,  $p_{\text{halo}}$  correspond to the probability that the star belongs to either the thin disk, thick disk or halo, respectively. Then,  $p$  and  $p_i$  are given by

$$p = f_1 p_1 + f_2 p_2 + f_3 p_3$$

and

$$p_i = \frac{1}{(2\pi)^{3/2} \sigma_{U_i} \sigma_{V_i} \sigma_{W_i}} \exp \left[ -\frac{U^2}{2\sigma_{U_i}^2} - \frac{(V - V_{\text{lag}})^2}{2\sigma_{V_i}^2} - \frac{W^2}{2\sigma_{W_i}^2} \right]. \quad (2)$$

The parameters  $f_i$  are the relative densities of thin disk, thick disk, and halo stars in the solar neighbourhood. Since there is an overlap of the Gaussian distributions in velocity space, the definition of the thin and thick disk populations is very sensitive to the choice of parameters defining the Gaussian distributions and the population fractions. There are several studies devoted to determining of the velocity ellipsoids of the thin

disk, thick disk, and halo components, as well as the population fractions in the solar neighbourhood. Here we compared studies by Soubiran et al. (2003) and Robin et al. (2003). We determined the probabilities using the values given in Table 3, where the velocity ellipsoids for the thin and thick disks were taken from Soubiran et al. (2003), and values from Robin et al. (2003) were used for the halo component. We also applied the same procedure to the thin disk, thick disk, and halo velocity dispersions and fractions from Robin et al. (2003):  $(\sigma_U, \sigma_V, \sigma_W)_{\text{thin}} = (43, 28, 18) \text{ km s}^{-1}$  and  $(\sigma_U, \sigma_V, \sigma_W)_{\text{thick}} = (67, 51, 42) \text{ km s}^{-1}$ ,  $f_{\text{thin}} = 0.93$  and  $f_{\text{thick}} = 0.07$ .

As a test, we applied the procedure, using Soubiran et al. (2003) and Robin et al. (2003), to the GCS stars, and the results are shown in Fig. 1. The decomposition of a larger sample into thin/thick disk makes the differences between Soubiran et al. (2003) and Robin et al. (2003) clearer. We considered that, if the probability of a star belonging to either the thin or thick disk is higher than 80%, then the star can be assigned to that component. If both  $p_{\text{thin}}$  and  $p_{\text{thick}}$  are lower than 80%, the star is classified as member of the intermediate population. Using velocity ellipsoids defined by Soubiran et al. (2003), we found that 81% of the GCS stars belong to the thin disk, 5% are thick disk stars, and 14% cannot be assigned to either of the components. The thin disk stars are restricted to  $V > -50 \text{ km s}^{-1}$ . Using Robin et al. (2003), the following fractions were found: 92%, 2%, and 6% are thin, thick, and intermediate stars, respectively, and the thin disk stars can rotate as slowly as  $V \sim -80 \text{ km s}^{-1}$ .

We then classified our 71 sample stars using velocity ellipsoids from Soubiran et al. (2003), and we found that 42 stars in the sample can be assigned to the thick disk, and 11 are more likely to be thin disk stars. The other 17 stars in the sample are intermediate between thin and thick disk components. Using Robin et al. (2003), we found that 16 stars in the sample belong to the thick disk, and 29 are more likely to be thin disk stars. The other 26 stars in the sample are not clearly members of either the thin or the thick disk components.

The same procedure (i.e., equations 1 and 2) was applied to the groups and stellar streams identified by Famaey et al. (2005). They applied a maximum-likelihood method to the kinematical data of 6691 K and M giants in the solar neighbourhood. They identified six kinematical groups: *i*) group Y, containing stars with ‘‘young’’ kinematics; *ii*) group HV, composed of high-velocity stars, which are probably mostly halo or thick disk stars; *iii*) group HyPl, the Hyades-Pleiades supercluster; *iv*) group Si, the Sirius moving group; *v*) group He, the Hercules stream; and *vi*) group B, which is composed of a ‘‘smooth’’ background in the UV plane, that are mostly thin disk stars. We obtained the probabilities of our sample stars belonging to these groups following the same procedure as above, assuming that the space velocities of each group follow a Gaussian distribution, with mean values, dispersions, and population fractions taken from Famaey et al.

As expected, neither of the sample stars belong to groups Y, HyPl, and Si, with probabilities below 1%. Only two stars have  $p_Y > 1\%$ : HD 35854 has  $p_Y = 6\%$  and HD 82943 has  $p_Y = 17\%$ , respectively. Despite 11 stars in the sample having a probability of belonging to the Hercules stream larger than 50%, neither of them satisfied our criteria  $p_{\text{He}} > 80\%$  to be assigned to this group. Six stars in our sample appear to belong to the B group ( $p_B > 80\%$ ), and 37 have kinematics compatible with the HV group ( $p_{\text{HV}} > 80\%$ ). The other 28 stars in the sample cannot be assigned clearly to either of these groups.

The right-hand panel in Fig. 1 presents the high velocity group, the B group and Hercules Stream stars, as classified by Famaey et al. (2005), and our sample star data overplotted in the

Table 2: Sample stars in common with the Geneva-Copenhagen survey (Holmberg et al. 2009).

Star	$R_{\min}$ (kpc)	$\Delta R_{\min}$ (kpc)	$R_{\max}$ (kpc)	$\Delta R_{\max}$ (kpc)	$e$	$\Delta e$	$Z_{\max}$ (kpc)	$\Delta Z_{\max}$ (kpc)
HD 9424	3.44	-0.35	8.28	0.47	0.41	0.07	0.08	0.03
HD 13386	4.74	-0.41	8.02	0.55	0.26	0.07	0.10	0.15
HD 25061	4.94	-0.23	9.20	0.44	0.30	0.04	0.04	0.15
HD 26151	6.39	-0.19	9.27	0.41	0.18	0.04	0.07	0.00
HD 35854	6.54	-0.36	8.02	0.53	0.10	0.06	0.17	-0.13
HD 82943	6.96	-0.25	8.23	0.41	0.08	0.05	0.03	0.16
HD 86249	8.00	0.51	8.78	0.21	0.05	-0.02	0.24	0.19
HD 90054 <sup>a</sup>	3.39	-0.33	8.02	0.50	0.41	0.06	0.18	0.13
HD 95338	2.98	-0.30	8.02	0.53	0.46	0.06	0.74	0.14
HD 104212	3.81	-0.63	7.98	0.53	0.35	0.11	0.24	0.36
HD 107509	3.43	-0.42	8.03	0.53	0.40	0.08	0.25	0.19
HD 148530	3.76	-0.20	9.12	0.59	0.42	0.04	0.51	0.17
HD 171999 <sup>b</sup>	3.94	-0.45	7.97	0.52	0.34	0.08	0.06	0.16
HD 180865	4.41	-0.30	8.02	0.50	0.29	0.06	0.11	0.15
HD 181433	6.72	0.07	10.06	0.41	0.20	0.01	0.27	-0.24
HD 218750	4.52	-0.54	8.16	0.53	0.29	0.08	0.30	-0.22
HD 224383	3.84	-0.38	8.59	0.44	0.38	0.07	0.09	0.02
Average		$-0.28 \pm 0.26$		$0.48 \pm 0.09$		$0.06 \pm 0.03$		$0.08 \pm 0.16$

Notes.  $\Delta$  = Our – GCS. <sup>(a)</sup> Binary. <sup>(b)</sup> Spectroscopic binary.

Table 3: Velocity ellipsoids for the thin disk, thick disk, and halo.

Component	$\sigma_U$	$\sigma_V$	$\sigma_W$	$V_{\text{lag}}$	Fraction
Thin disk <sup>a</sup>	39	20	20	-7	0.85
Thick disk <sup>a</sup>	63	39	39	-46	0.15
Halo <sup>b</sup>	131	106	85	-220	0.006

Notes. <sup>(a)</sup> Soubiran et al. (2003). <sup>(b)</sup> Robin et al. (2003). <sup>(c)</sup> Famaey et al. (2005).

Toomre diagram. In Table 5 the kinematics of our sample are compared with the data for 6030 stars from Famaey et al. (2005), where all the samples analysed show low maximum height above the plane. It appears that our sample is compatible with the high-velocity group (HV), and might be identified with that subpopulation. This group is probably composed of halo or thick-disk stars, and represents about 10% of the whole sample analysed by Famaey et al. (2005). Most stars assigned to the thick disk component, following the Soubiran et al. (2003) velocity distributions, are also members of the HV group.

The probabilities assumed for classifying the present 71 sample stars are those obtained with Soubiran et al. (2003) velocity ellipsoids, and not those suggested by Robin et al. (2003) (that give a low fraction of thick disk stars  $f_{\text{thick}} = 0.07$ ). A higher fraction of nearby thick disk stars is supported by recent studies of the SDSS data (Jurić et al. 2008). Moreover, membership probabilities obtained with Soubiran et al. (2003) criteria are in better agreement with the more detailed analysis of the velocity space by Famaey et al. (2005). The final probabilities  $p_{\text{thin}}$  and  $p_{\text{thick}}$  are reported in Table 12. In Table 4, we report the mean ages (Sect. 5.5), metallicities (Sect. 5.3),  $[\alpha/\text{Fe}]$  (Sect. 6), space velocities, eccentricities, and maximum height above the Galactic plane for each of the populations: thin disk, thick disk, and intermediate. The stars with intermediate properties are so classified for having intermediate eccentricity,  $V$  velocity,  $Z_{\max}$ , and  $R_{\text{m}}$  relative to the thick and thin disks.

## 5. Stellar parameters

A common method for deriving of stellar parameters relies on the abundances derived from Fe I and Fe II lines, by requiring excitation and ionization equilibria. In this work it was not assumed *a priori* that the absolute equilibria are reached, since this procedure could hide non-LTE effects, leading to misleading parameters. This choice is justified by previous work, which suggests that deviations from LTE are present in metal-rich dwarf stars (e.g. Feltzing & Gustafsson 1998; Meléndez & Ramírez 2005). Therefore, the stellar temperatures and surface gravities were obtained without recourse to the Fe I and Fe II lines as follows.

- i*) The effective temperatures were calculated from the  $(V-K_S)$  colour using the Casagrande et al. (2010, hereafter CRM10) colour-temperature relations, as described in Sect. 5.1.
- ii*) Then,  $\log g$  is derived from masses and parallaxes. Using the HIPPARCOS parallaxes and the stellar masses from the Yonsei-Yale evolutionary tracks (Demarque et al. 2004), hereafter  $Y^2$ , the surface gravities were derived following the procedure presented in Sect. 5.2.
- iii*) We used the metallicities from Geneva photometry as first guesses in steps *i* and *ii*.
- iv*) Then, fixing  $T_{\text{eff}}$  and  $\log g$ , the iron abundance and microturbulence velocity were derived from Fe I and Fe II lines, through local thermodynamic equilibrium (LTE) analysis, using the MARCS model atmospheres (Gustafsson et al. 2008). The microturbulence velocity was obtained by imposing constant iron abundance as a function of equivalent width (except for the cooler stars). The iron abundance and microturbulence velocity determinations are described in detail in Sect. 5.3.
- v*) The Geneva metallicity was then replaced by the new iron abundance, to go through the whole iteration process
- vi*) the procedure was repeated until there were no significant changes in  $(T_{\text{eff}}, \log g, [\text{Fe}/\text{H}])$ .

The changes on temperatures and gravities due to changes on metallicities are small, but not zero. Therefore, the procedure includes iteration to keep internal consistency. The final photometric parameters were tested against excitation and ionization

Table 4: Mean data for the thin, thick, and intermediate populations.

Group	Age (Gyr)	[Fe/H] (dex)	[ $\alpha$ /Fe] (dex)	$R_m^a$ (kpc)	$U_{\text{LSR}}^b$ (km s <sup>-1</sup> )	$V_{\text{LSR}}^b$ (km s <sup>-1</sup> )	$W_{\text{LSR}}^b$ (km s <sup>-1</sup> )	$e$	$Z_{\text{max}}$ (kpc)
Thin disk	7.8 ± 3.5	0.20 ± 0.22	-0.01 ± 0.05	8.2 ± 0.6	-10 ± 51	-19 ± 16	-11 ± 15	0.20 ± 0.08	0.21 ± 0.16
Thick disk	7.5 ± 3.1	0.22 ± 0.17	0.00 ± 0.04	6.3 ± 0.4	36 ± 43	-84 ± 17	-21 ± 23	0.40 ± 0.07	0.38 ± 0.40
Intermediate	6.8 ± 2.9	0.29 ± 0.17	-0.02 ± 0.03	7.3 ± 0.5	37 ± 61	-48 ± 13	-20 ± 14	0.29 ± 0.05	0.28 ± 0.22

**Notes.** <sup>(a)</sup> Mean Galactocentric distance,  $R_m = (R_{\text{max}} + R_{\text{min}})/2$ . <sup>(b)</sup> Space velocities with respect to the local standard of rest.

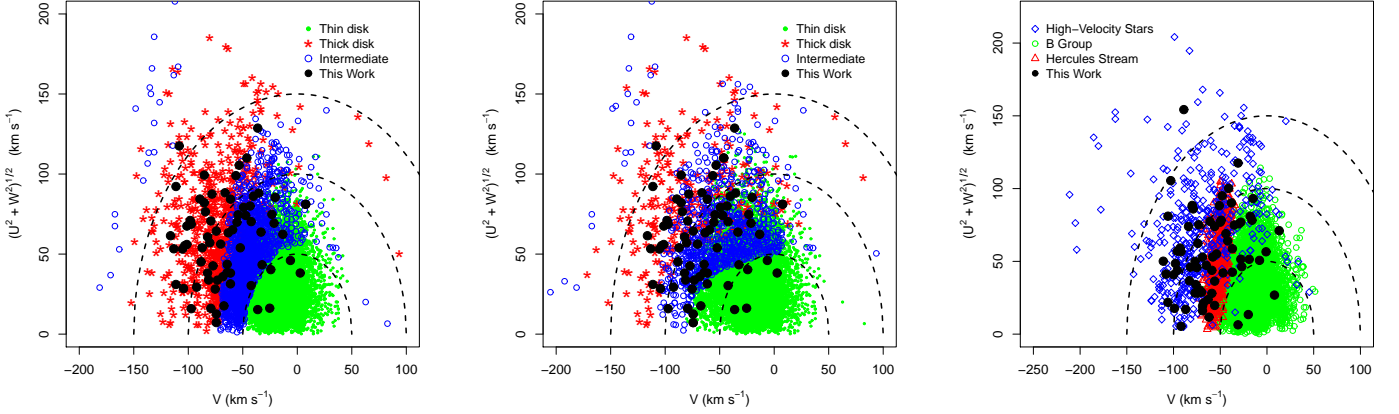


Fig. 1: Toomre diagram of GCS stars. *Left and middle panels:* The thin/thick disk decomposition of GCS stars was performed using the velocity dispersions and star fractions from Soubiran et al. (2003) (*left*) and from Robin et al. (2003) (*middle*). The thin, thick, and intermediate stars of the GCS are represented by green dots, red stars, and open blue circles, respectively. The dashed lines indicate the total space velocity,  $v_{\text{total}} = \sqrt{U^2 + V^2 + W^2}$ , in steps of 50 km s<sup>-1</sup>. *Right panel:* Toomre diagram showing the groups identified by Famaey et al. (2005): the Hercules stream (red open triangles), high-velocity stars (blue open diamonds), and B-group stars (green open circles). In all panels the present sample is indicated by black dots.

Table 5: Mean kinematical data for our sample, compared with kinematic groups studied by Famaey et al. (2005).

Kinematic group	$\langle U(\text{km s}^{-1}) \rangle$	$\langle V(\text{km s}^{-1}) \rangle$	$\langle W(\text{km s}^{-1}) \rangle$	$\langle Z_{\text{max}}(\text{pc}) \rangle$
present sample	17.6 (55.0)	-60.1 (29.7)	-10.6 (21.0)	330.0
HV Stars	18.5 (62.6)	-53.3 (37.2)	-6.6 (45.9)	208.1
B Group	2.9 (31.8)	-15.2 (17.6)	-8.2 (16.3)	196.1
Hercules Stream	42.1 (25.3)	-51.6 ( 7.1)	-8.1 (15.4)	132.9

**Notes.** <sup>0</sup> HV refers to high-velocity stars. Standard deviations are presented in parenthesis.

equilibria, and  $T_{\text{eff}}$  and  $\log g$  were further adjusted if necessary, as shown in Sect. 5.4. Only two stars in the sample required adjustments to be in satisfactory spectroscopic equilibrium.

We estimated ages for the sample stars, using the  $Y^2$  isochrones. Details about the determination of stellar masses and ages are given in Sect. 5.5. Final considerations about the parameter determinations and comparison with other studies are presented in Sect. 5.6.

### 5.1. Temperatures

The basic photometric data used in temperature determinations are presented in Table 1: photometric temperatures from Geneva photometry;  $V$  magnitudes (ESA 1997);  $J$  and  $K_S$  magnitudes from 2MASS (Skrutskie et al. 2006); Bolometric correction  $BC_V$  from Alonso et al. (1995) (see Sect. 5.2); and HIPPARCOS parallaxes  $\pi$  (ESA 1997). Errors of about 0.02 mag

apply to  $V$  magnitudes; the errors on the other magnitudes are reported in Table 1. The sample stars are all within 90 pc of the Sun and since interstellar reddening is usually zero for stars lying within 100 pc of the Sun (Schuster & Nissen 1989), no reddening corrections were applied. We checked this assumption using the extinction law by Chen et al. (1998), and we verified that the maximum reddening correction would be 0.1 mag for HD 104212. This level of extinction would raise the temperature by 130 K. Even so, excitation equilibrium was reached for this star (see Sect. 5.4). Thus, we adopted  $A_V = 0$  for all the sample stars.

We derived temperatures from CRM10’s colour-temperature calibrations. The results were compared with those determined with the widely adopted relations from Alonso et al. (1996, hereafter AAM96) and with temperatures from Geneva photometry, which are also available for all the sample stars.



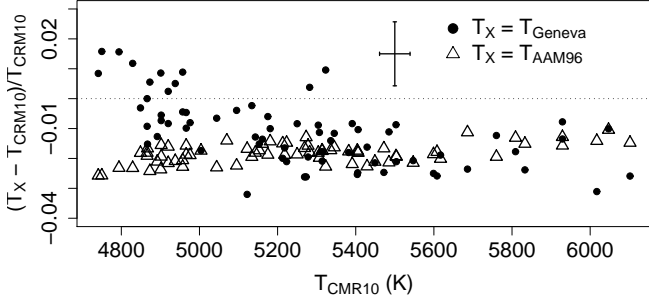


Fig. 2: Photometric temperatures. The temperatures from CRM10 calibrations are compared with those from AAM96 relations (open triangles) and from Geneva photometry (filled circles). CRM10 temperatures are about 2% ( $\sim 90$  K) hotter than AAM96 ones.

CRM10 provide colour-temperature relations for Johnson V and 2MASS J and  $K_S$  magnitudes, so no magnitude system transformations are needed. To determine the photometric  $T_{(J-K)}$  and  $T_{(V-K)}$  temperatures from the colour-temperature calibrations described in AAM96, the following photometric system transformations were used. The J,  $K_S$  magnitudes and colours were transformed from the 2MASS system to CIT (California Institute of Technology) system, and from the latter to TCS (Telescopio Carlos Sánchez) system, with the relations established by Carpenter (2001) and Alonso et al. (1994). The transformations between the Johnson and TCS systems used the relations presented in Alonso et al. (1994).

Figure 2 presents the comparison between photometric temperatures. AAM96 relations give temperatures about 2% ( $\sim 90$  K) lower than CRM10 ones, in agreement with differences found by CRM10 between these two calibrations. As discussed in CRM10, the main source of differences between photometric  $T_{\text{eff}}$  scales is the absolute calibration of the photometric systems, which is essential when setting the zero point of the scale. The estimated zero point of the CRM10 scale is defined by a sample of solar twins, resulting in zero-point uncertainties of  $\sim 15$  K. For AAM96 calibrations, this uncertainty is  $\sim 100$  K (Casagrande et al. 2006, 2010). Moreover, AAM96 calibrations require photometric system transformations, which can introduce unnecessary errors. Therefore, the CRM10 calibrations were chosen for the effective temperature, and the  $(V - K_S)$  colour calibration was preferred over the other colours, owing to the extended base line, a confirmed lower  $\sigma(T_{\text{eff}}) \sim 25$  K, and smaller dependence with  $[\text{Fe}/\text{H}]$ .

The internal errors in temperatures were computed considering the uncertainties in magnitudes and metallicities:

$$\sigma_{T_{\text{eff}}} = \frac{5040}{\theta^2} \left[ \left( \frac{\partial \theta}{\partial [\text{Fe}/\text{H}]} \sigma_{[\text{Fe}/\text{H}]} \right)^2 + \left( \frac{\partial \theta}{\partial (V-K)} \sigma_{(V-K)} \right)^2 \right]^{1/2} \quad (3)$$

where  $\sigma_{(V-K)}$  is the quadratic sum of errors in V and  $K_S$  magnitudes, and  $\theta (= 5040/T_{\text{eff}})$  is a function of  $(V - K)$  and  $[\text{Fe}/\text{H}]$ , as given in CRM10. Uncertainties in the zero point of the scale (15 K) and the calibration deviations (25 K, as given in Table 4 of CRM10) were added quadratically to the internal error. The final temperatures and errors are presented in Table 13.

## 5.2. Surface gravities

The trigonometric surface gravities,  $\log g$ , were derived from HIPPARCOS parallaxes,  $\pi$ , through the standard formula

$$\log \left( \frac{g_{\star}}{g_{\odot}} \right) = 4 \log \left( \frac{T_{\text{eff},\star}}{T_{\text{eff},\odot}} \right) + 0.4(\mathcal{M}_{\text{Bol},\star} - \mathcal{M}_{\text{Bol},\odot}) + \log \left( \frac{M_{\star}}{M_{\odot}} \right) \quad (4)$$

where  $T_{\text{eff},\star}$  and  $M_{\star}$  are the stellar temperature and mass, respectively, and the bolometric magnitude,  $\mathcal{M}_{\text{Bol},\star}$ , is given by

$$\mathcal{M}_{\text{Bol},\star} = V - A_V + BC_V + 5 \log \pi + 5.$$

The following values were adopted for the Sun:  $T_{\text{eff},\odot} = 5777$  K,  $\mathcal{M}_{\text{Bol},\odot} = 4.75$  (Barbuy 2007) and  $\log g_{\odot} = 4.44$ . We used bolometric corrections  $BC_V$  from Alonso et al. (1995), where  $(V-K)_{\odot} = 1.486$ ,  $BC_{V,\odot} = -0.08$  were adopted.

Errors in gravities were calculated using the error propagation equation, derived from equation 4:

$$\sigma_{\log g}^2 = \sigma_M^2 \cdot k^2 \left( \frac{M_{\odot}}{M} \right)^2 + \sigma_{T_{\text{eff}}}^2 \cdot k^2 \left( \frac{4}{T_{\text{eff}}} \right)^2 + \sigma_{\pi}^2 \cdot k^2 \left( \frac{5}{\pi} \right)^2 + 2 \sigma_{M,T_{\text{eff}}}^2 \cdot k^2 \left( \frac{M_{\odot}}{M} \right) \left( \frac{4}{T_{\text{eff}}} \right) \quad (5)$$

where  $k = \log e = 0.4343$ , and errors in  $BC_V$  and magnitudes were considered to be small. The variables  $\sigma_M$ ,  $\sigma_{T_{\text{eff}}}$ , and  $\sigma_{\pi}$  are errors in masses, temperatures, and parallaxes, respectively. Since we used the temperatures to get the masses from isochrones, the covariance between  $T_{\text{eff}}$  and mass,  $\sigma_{M,T_{\text{eff}}}$ , does not vanish. For each star, we took all the possible solutions  $[M_i, T_{\text{eff},i}]$  within the error bars from the evolutionary tracks. Given that  $\bar{M}$ ,  $\bar{T}_{\text{eff}}$  are the respective mean values, the covariance can be obtained through

$$\sigma_{M,T_{\text{eff}}} = \left\langle (M_i - \bar{M}) \cdot (T_{\text{eff},i} - \bar{T}_{\text{eff}}) \right\rangle. \quad (6)$$

Table 6 presents the variations in  $\log g$  with temperature, masses,  $E(B-V)$ , and  $[\text{Fe}/\text{H}]$ . A temperature change of  $-2\%$  ( $\sim 100$  K), which corresponds to the difference between CRM10 and AAM96 calibrations, would lead to lower stellar masses by 4% in average. The overall change in gravities is  $-0.05$  dex on average. Despite the uncertainties involved in the determination of stellar masses, the effect on gravity is not significant: a 5% change in the masses would change gravities by only 0.02 dex. As described in Sect. 5.5, the masses estimated in this work have internal errors of about 3% and accuracy of 4%, resulting in a total uncertainty of about 5%. Effects of reddening corrections and changes in  $[\text{Fe}/\text{H}]$  are not significant (0.01 and  $< 0.005$  dex, respectively).

We checked the consistency between trigonometric gravities and evolutionary gravities. For this comparison, we used both  $Y^2$  and Padova isochrones (Girardi et al. 2000). Padova gravities were obtained using the tool PARAM<sup>1</sup> (da Silva et al. 2006). The  $Y^2$  gravities are the mean values of all the solutions within  $T_{\text{eff}} \pm \sigma_{T_{\text{eff}}}$  and  $\mathcal{M}_{\text{abs}} \pm \sigma_{\mathcal{M}_{\text{abs}}}$ , where  $\sigma_{T_{\text{eff}}}$  and  $\sigma_{\mathcal{M}_{\text{abs}}}$  are the errors in temperatures and absolute magnitudes. The agreement between both evolutionary ( $Y^2$ , Padova) gravities and trigonometric gravities is excellent, as shown in Fig. 3. A large difference of  $\sim 0.4$  dex between HIPPARCOS and isochrones gravities was found for HD 201237. The photometry and/or Galactic

<sup>1</sup> <http://stev.oapd.inaf.it/cgi-bin/param>

Table 6: Gravity variations with stellar parameters

	$\Delta T_{\text{eff}}$ (-2 %)	$\Delta \text{Mass}$ (-5 %)	$\Delta E(B - V)$ (+0.05 mag)	$\Delta [\text{Fe}/\text{H}]$ (-0.30 dex)
$\Delta \log g$ (dex)	-0.05	-0.02	0.01	< 0.01

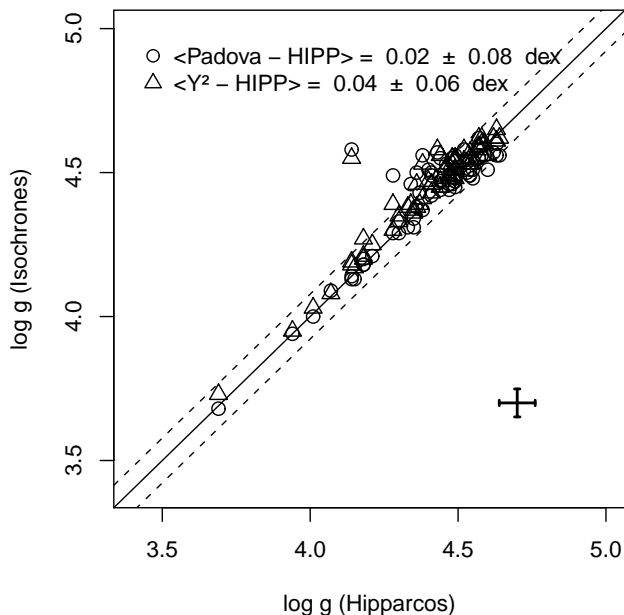


Fig. 3: Comparison between trigonometric gravities from HIPPARCOS parallaxes and isochrone gravities. The open triangles represent the gravities obtained from  $Y^2$  evolutionary tracks, and gravities from Padova isochrones are indicated by open circles. Solid and dashed lines show the very good agreement, with variations within  $\pm 0.05$  dex.

extinction should not be the source of this discrepancy. This star has good quality photometry from the 2MASS catalogue; i.e., the photometric quality flags are set to A, and the errors on the magnitudes are  $\sim 0.02$  mag. The reddening correction for this star is only  $E(B-V) \sim 0.04$  mag, following the law by Chen et al. (1998), and this level of correction should not affect the stellar parameter determinations significantly. On the other hand, the HIPPARCOS parallax has a large error ( $\sim 19\%$ ), which leads to an uncertainty of  $\sim 0.16$  dex on gravity. Therefore, the parallax error is the most probable source of the discrepancy between HIPPARCOS and isochrones gravities. The stellar parameters found by Pompéia et al. (2002) for this star,  $(T_{\text{eff}}, \log g, [\text{Fe}/\text{H}]) = (4950 \text{ K}, 4.10, -0.05)$ , are in good agreement with those found in this work,  $(4829 \text{ K}, 4.14, 0.00)$ .

The final  $T_{\text{eff}}$  and  $\log g$  parameters are presented in Fig. 4, where  $Y^2$  evolutionary tracks are shown for comparison.

### 5.3. Metallicities

We performed an LTE analysis to obtain the iron abundances from the measured equivalent widths. The calculations were carried out using the Meudon code ABON2 (Spite 1967, and updates implemented since then). We used the MARCS 1D hydro-

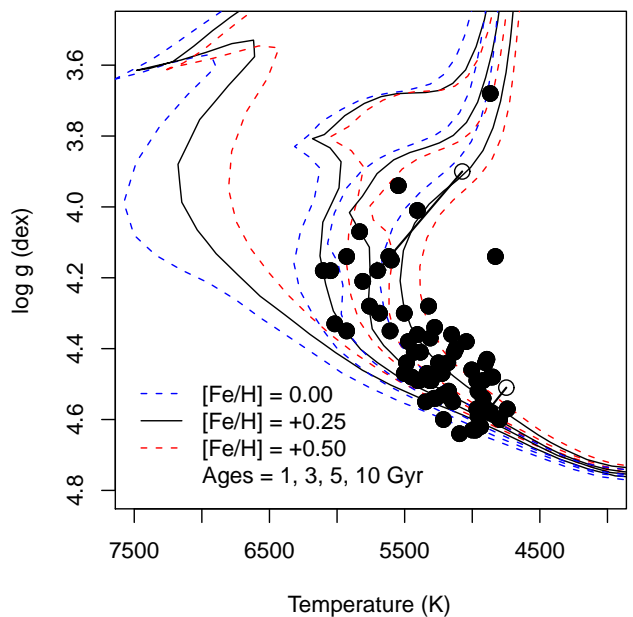


Fig. 4: Temperatures vs. gravities.  $Y^2$  isochrones representing different ages and metallicities are shown. The lines connecting an open and a filled circle depict changes in temperature and gravity of HD 94374 and HD 182572 to achieve excitation equilibrium (see text). The open circles indicate photometric temperatures obtained as described in Sect. 5.1; the filled circles correspond to the excitation-equilibrium values, which were adopted for these two stars.

static model atmospheres (Gustafsson et al. 2008), obtained by interpolation for the appropriate parameters of the sample stars.

The list of neutral and ionized iron lines used in this work were based on the lists from Castro et al. (1997), Bensby et al. (2003) and Meléndez et al. (2009). The oscillator strengths,  $\log gf$ , adopted in this work were fitted in order to reproduce the solar iron abundance  $(\text{Fe}/\text{H})_{\odot} = 7.5^2$  (Grevesse & Sauval 1998), using  $T_{\text{eff}\odot} = 5777 \text{ K}$ ,  $\log g_{\odot} = 4.44$ , and  $\xi_{\odot} = 0.9 \text{ km s}^{-1}$ . The damping constants were computed when possible, using the collisional broadening theory of Barklem et al. (1998, 2000) and Barklem & Aspelund-Johansson (2005, and references therein).

The final iron line list comprises only lines that

- i) are free of blends. We used an atlas of the solar photospheric spectrum (Wallace et al. 1998) and the VALD line lists (Kupka et al. 1999) to check for possible blends, and blended lines were discarded;
- ii) have solar  $W_{\lambda} < 100 \text{ mÅ}$ . For this range of  $W_{\lambda}$ , the astrophysical  $\log gf$  values obtained from the solar equivalent widths are more reliable (for stronger lines oscillator strengths and broadening of wings have competing effects); and
- iii) give systematically reliable abundances for the sample stars.

Given that  $\langle A \rangle_i$  is the iron abundance of each star, and  $A_{\lambda i}$  is the abundance derived from an individual line, we checked the “quality” of the line by computing  $A_{\lambda i} - \langle A \rangle_i$  for all the

<sup>2</sup>  $(X/H) = \log(N_X/N_H) - 12$



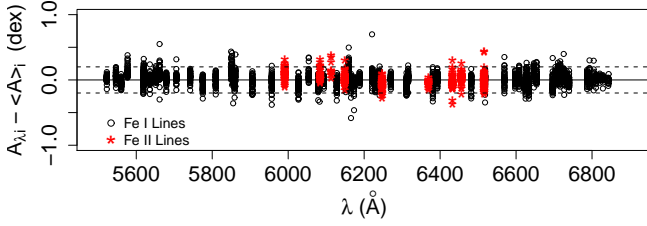


Fig. 5: Process of selection for stable Fe I and Fe II lines. The iron abundance of each star,  $\langle A \rangle_i$ , is the average of abundances derived from individual lines,  $A_{\lambda i}$ .  $A_{\lambda i} - \langle A \rangle_i$  values indicate deviations from the mean abundance value for each star. Fe I and Fe II lines are indicated as open circles and red stars, respectively.

sample stars (Fig. 5). This approach allows us to detect and exclude lines that give abundances systematically higher or lower than the abundance of the star by 0.15 dex and lines that seem to lead to inaccurate abundance values (deviation in  $A_{\lambda i} - \langle A \rangle_i$  larger than 0.12 dex).

Atomic data adopted for the final iron line list are given in Table A.4. The equivalent widths of iron lines were measured using the automatic code ARES<sup>3</sup> developed by Sousa et al. (2007). Given a reference line list and a list of input configuration parameters, ARES fits a continuum and measures  $W_\lambda$  by fitting a Gaussian profile.

We tested the dependence of  $W_\lambda$  on the choice of the ARES’s input parameters by comparing measurements made with different values, in particular the parameter required for the continuum definition (*rejt*) and the parameter that defines the wavelength interval around the line where the computation will be conducted (*space*). By considering different values for these parameters in the intervals  $0.993 < rejt < 0.999$  and  $2 < space < 5 \text{ \AA}$ , we obtained  $\sigma_{W_\lambda}$ , which is the standard deviation of the measurements. Despite the majority of the lines giving a stable result under different configurations, we found that some lines are very sensitive to the choice of these parameters. The differences between measurements made with different values of *rejt* and *space* can be as high as  $\sigma_{W_\lambda} \sim 15\text{--}20\%$ . To avoid the effect of these lines in computing of the final metallicity, for each line with  $W_\lambda \pm \sigma_{W_\lambda}$ , we computed the iron abundance  $[\text{Fe}/\text{H}] \pm \sigma_{[\text{Fe}/\text{H}]}$ . The final  $[\text{Fe}/\text{H}]$  of each star was then considered as the weighted mean of the abundances, where  $w = (1/\sigma_{[\text{Fe}/\text{H}]})$  were used as weights for each line.

The reliability of the ARES measurements was confirmed by comparing equivalent widths of iron lines measured with both ARES and the task SPLIT in the IRAF context. Figures 6 and 7 present the good agreement between  $W_\lambda$ s measurements for the Sun and the stars HD 11608, HD 77338, and HD 81767.

We employed the equivalent widths of Fe I lines to derive the microturbulence velocity,  $\xi$ , by requiring independence between abundances and the reduced equivalent width,  $\log(W_\lambda/\lambda)$ . Only lines with  $20 < W_\lambda < 100 \text{ m\AA}$  were used, since fainter lines show some scatter in the comparison between ARES and SPLIT, and stronger lines are not well fitted by Gaussian profiles. No clear  $\xi$  velocities were found for our cooler stars ( $T_{\text{eff}} < 5000 \text{ K}$ ). We considered that  $\xi$  can be defined as a function of temper-

ature and gravity, and using stars with  $T_{\text{eff}} > 5200 \text{ K}$ , we defined  $\xi = f(T_{\text{eff}}, \log g)$  and then extrapolated this function to  $T_{\text{eff}} < 5200 \text{ K}$ . We adopted  $0.3 \text{ km s}^{-1}$  from the extrapolation of our fit. The same problem was found by Feltzing & Gustafsson (1998) for their K dwarfs, and they adopted a constant value of  $1 \text{ km s}^{-1}$ . We found that this value is too high for our sample, leading to lower metallicities in this temperature range and, consequently, to a positive gradient  $[\text{Fe}/\text{H}]$  vs.  $T_{\text{eff}}$ . A variation of  $\Delta\xi = +0.2 \text{ km s}^{-1}$  leads to  $\Delta[\text{Fe I, II}/\text{H}] = -0.05 \text{ dex}$ . The errors in  $\xi$  were calculated considering the uncertainty in the slope of abundance vs.  $W_\lambda$ , and are typically  $0.1 \text{ km s}^{-1}$ .

To compute the errors in the final metallicity, the following sources of uncertainties were taken into account: *i*) uncertainties in the stellar parameters [ $T_{\text{eff}}$ ,  $v_t$ ,  $\log g$ ]; *ii*) errors in the  $W_\lambda$ s measurements, which were estimated by considering several configurations of the ARES code as described above; and *iii*) uncertainties in  $\log gf$  values, which were computed by considering errors in the solar  $W_\lambda$ s. The total errors are  $\sim 0.05$  for  $[\text{Fe I}/\text{H}]$  and  $0.09 \text{ dex}$  for  $[\text{Fe II}/\text{H}]$ .

### 5.3.1. Metallicities from two different codes

We proceeded with all the calculations described above using both the code by the Uppsala group BSYN/EQWI (Edvardsson et al. 1993, and updates since then) and the Meudon code ABON2 (Spite 1967, and updates implemented since then). All steps of the calculation were carefully compared: optical depths of lines, continuum opacities  $\kappa_c$ , line broadening, and final abundances.

The dominating opacity source is the  $\text{H}^-$  bound-free absorption. The two codes consider different calculations for the  $\text{H}^-$  photo-detachment cross section  $\sigma_\lambda$ . The ABON2 code (Spite 1967) adopts Geltman (1962) calculations, represented by the polynomial expressions from Gingerich (1964), while cross sections from Wishart (1979) are adopted in the BSYN/EQWI code (Edvardsson et al. 1993). Using these sources and considering a Fe I line at  $5861 \text{ \AA}$  and the solar atmosphere model, we found that differences in the continuum absorption are up to 4% in the upper atmospheric layers ( $\tau_5 < -1$ ), and less than 1% in the bottom of the photosphere ( $\tau_5 > 0$ ). We updated the ABON2 code (Spite 1967) using new cross sections calculations from John (1988), which improve the agreement of  $\kappa_c$  between these two codes to  $< 1\%$  at the upper layers with  $\tau_5 < -1$  and  $\sim 2\%$  at  $\tau_5 > 0$  layers (Fig. 8).

The line opacity ( $\kappa_l$ ) calculated for an Fe I line at  $5861 \text{ \AA}$  is shown in Fig. 8 with a solar model. We found that the ratio between line opacities,  $\kappa_{l, \text{BSYN}}/\kappa_{l, \text{ABON2}}$ , decreases with optical depth. An agreement between their values in the two codes is found at  $\log \tau_5 \approx 0$ . The small discrepancy is mainly due to differences in the van der Waals broadening determinations. The ratio  $\kappa_l/(\kappa_l + \kappa_c)$  is within 1% at layers with  $\tau_5 < -1$ .

The same analysis was carried out for other lines at different wavelengths and atmosphere models. Despite the small trends with  $\lambda$  and  $T_{\text{eff}}$ , Table 7 shows that the differences found between metallicities obtained with the two codes are within 0.02 dex.

### 5.4. Checks on excitation and ionization equilibria

Since we are using temperatures from photometric scales and trigonometric gravities, it is interesting to check whether excitation and ionization equilibria are reached. For each star, we plotted iron abundances vs. the excitation potential  $\chi_{\text{exc}}$  (eV) and performed a linear fit between these two quantities (Fig. 9 shows

<sup>3</sup> <http://www.astro.up.pt/~sousasag/ares/>

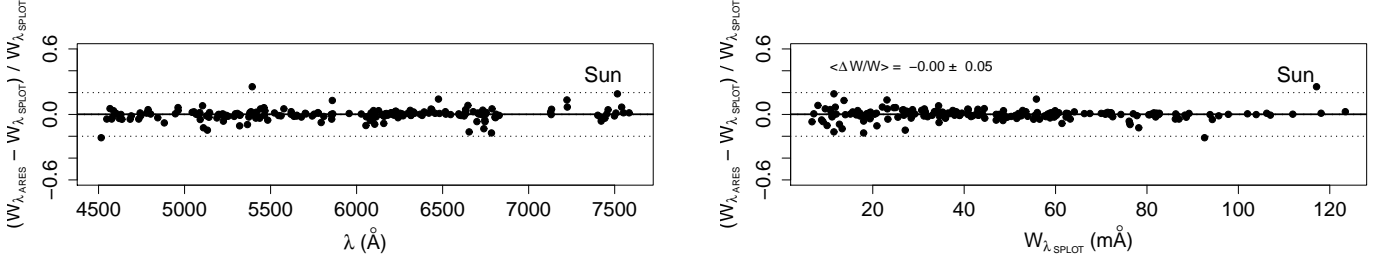


Fig. 6: Equivalent widths measurements from ARES and IRAF for the solar spectrum. The relative differences,  $(W_{\lambda_{\text{ARES}}} - W_{\lambda_{\text{IRAF}}})/W_{\lambda_{\text{IRAF}}}$ , are given as a function of wavelength (*left*) and  $W_{\lambda_{\text{IRAF}}}$  (*right*).

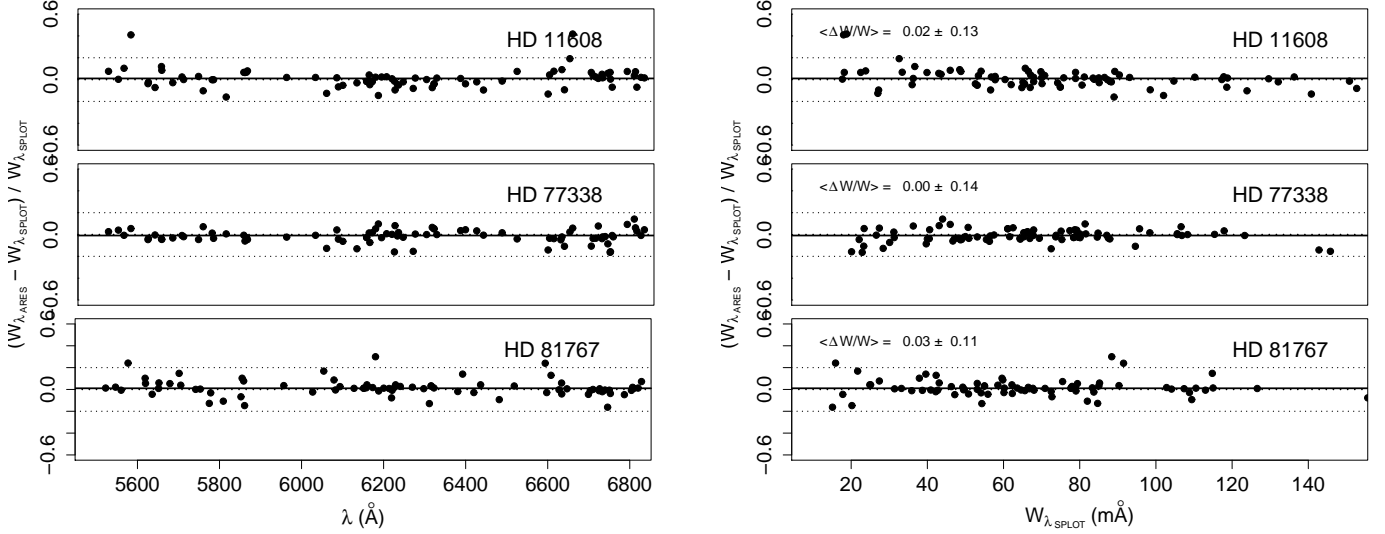


Fig. 7: Same as Fig. 6 for the stars HD 11608, HD 77338, and HD 81767.

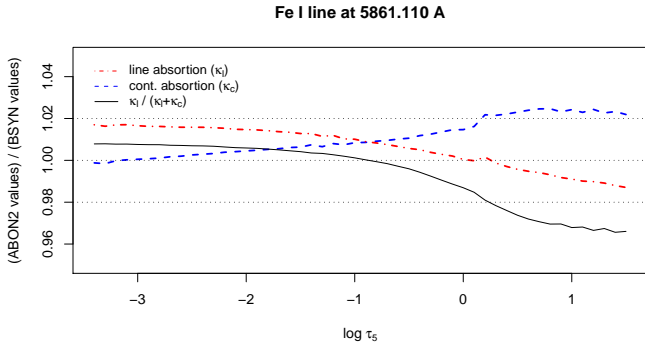


Fig. 8: Ratio of opacities computed using the BSYN/EQWI (Edvardsson et al. 1993) and ABON2 (Spite 1967) codes for an Fe I line at  $\lambda = 5861.11 \text{ \AA}$  for the solar model.

HD 26151 as an example). The excitation equilibria is indicated by the independence between abundances and  $\chi_{exc}$ ; i. e., the slope  $b$  must be zero. Figure 10 presents the slope  $b$  as a function of temperature, gravity, and metallicity for all the sample stars. The slope exceeded  $2\sigma$  from the mean value for two stars: HD 94374 and HD 182572. HD 182572 is a known variable,

Table 7: Abundances obtained with two different codes

Star	$T_{\text{eff}}$ (K)	$\log g$	$\Delta[\text{Fe I}/\text{H}]^a$	$\Delta[\text{Fe II}/\text{H}]^a$
Sun	5777	4.44	0.00	0.00
HD 15133	5223	4.47	0.01	0.02
HD 77338	5346	4.55	0.01	0.01
HD 90054	6047	4.18	0.01	0.00
HD 177374	5044	4.38	0.01	0.02

Notes. <sup>(a)</sup>  $\Delta[\text{Fe}/\text{H}] = [\text{Fe}/\text{H}]_{\text{BSYN}} - [\text{Fe}/\text{H}]_{\text{ABON2}}$ .

with an amplitude variation smaller than 0.2 mag. The photometric calibrations give  $T_{\text{eff}} \approx 5070 \text{ K}$ , and the excitation temperature (5700 K) was adopted for this star. For G 161-029 no parallax measurement is available. Therefore spectroscopic  $T_{\text{eff}}$  and  $\log g$  were adopted for these three stars.

In addition to these outlier stars in Fig. 10, we found small trends between the slope  $b$  and temperatures/gravities. This was also found by Feltzing & Gustafsson (1998) in their analysis of 47 metal-rich stars. On the other hand, the trend between  $b$  and  $[\text{Fe}/\text{H}]$  is very small; thus, the effect of choosing photometric temperatures over excitation ones on the final metallicities should be negligible. We quantified this effect by obtaining the excitation temperatures by requiring zero slope from the

excitation energy balance diagram, and we compared the excitation and photometric temperatures, as shown in Fig. 12. The excitation temperatures agree well with the photometric ones. Differences between temperatures are all below  $\pm 5\%$ , except for the stars HD 94371 and HD 182572, for which the excitation temperatures were adopted. The mean difference is only 0.7%, with a standard deviation of 2.5%. For  $[\text{Fe}/\text{H}] \gtrsim 0.4$ , the photometric temperatures are systematically higher than excitation temperatures by an amount of 2% in average. If we consider 2% lower temperatures in these cases, the resulting change in abundance is  $\sim -0.05$  dex. Finally, in Fig. 11, we show that the iron abundances derived from Fe I show no obvious trend with  $T_{\text{eff}}$ .

Ionization equilibria, indicated by the difference between Fe I and Fe II abundances, is shown in Fig. 13 for all the sample stars. We found an apparent overionization as compared to expectations from LTE calculations for the cooler stars ( $T_{\text{eff}} \leq 5200$  K) in the sample, with an upper limit of  $[\text{Fe II}-\text{Fe I}] < 0.2$  dex. Even though lines of ionized iron atoms are less susceptible to non-LTE effects than Fe I (Thévenin & Idiart 1999), we considered the abundances derived from Fe I lines to be the final metallicities of our stars, since Fe I lines are more numerous.

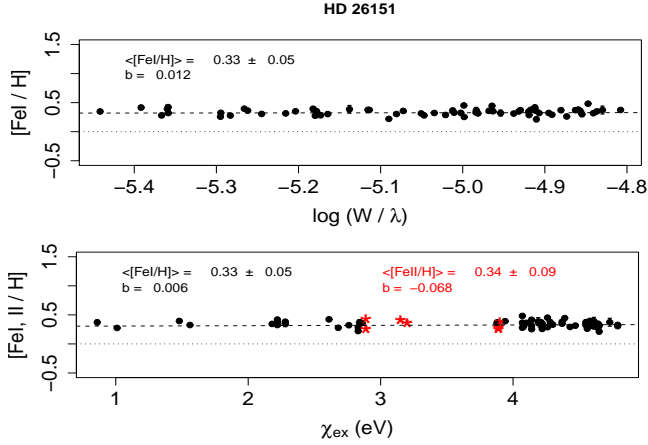


Fig. 9: Abundances versus normalized equivalent widths,  $\log(W/\lambda)$  (*top*), and excitation/ionization equilibrium (*bottom*) shown for HD 26151, as an example. Red stars represent Fe II lines. The Fe I and Fe II abundances and linear coefficients  $b$  are given in the plots.

### 5.5. Stellar masses and ages

Isochrone fitting techniques can provide estimates of stellar masses and ages. Allende Prieto & Lambert (1999) compared masses derived from interpolation of isochrones and the direct estimates from observations in eclipsing spectroscopic binaries, and they concluded that masses can be estimated with uncertainties below 8%. More recently, Meléndez et al. (2011, in prep.) show that masses and ages can be estimated with even higher accuracy, provided the isochrones are well calibrated to reproduce the solar ages and masses.

Therefore, we used a grid of Yonsei-Yale isochrones to determine the masses and ages for the sample stars. The isochrone points were characterized by the effective temperature ( $T_{\text{eff}}$ ), the absolute magnitude ( $M_V$ ), and the metallicity ( $[\text{Fe}/\text{H}]$ ). Using

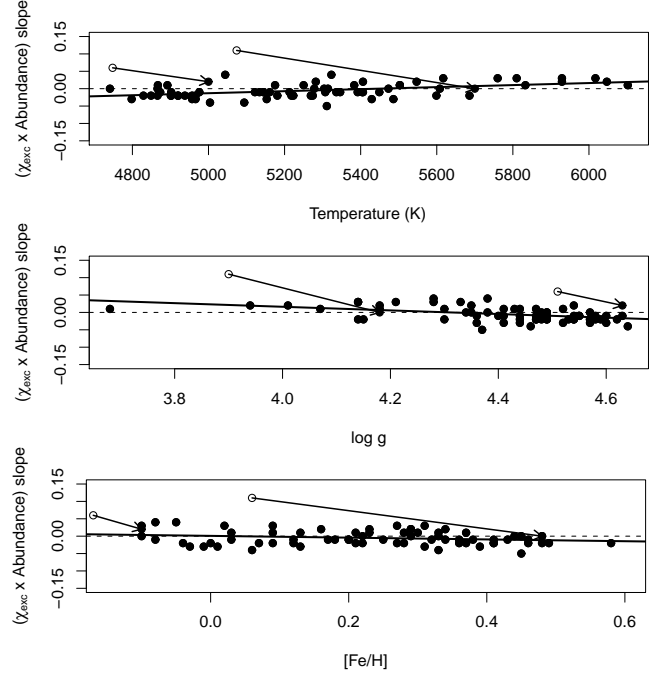


Fig. 10: Excitation equilibrium as a function of temperature (*top*), gravity (*middle*), and metallicity (*bottom*). The dashed line indicates the perfect excitation equilibrium. The arrows indicate changes in temperature and gravity of HD 94374 and HD 182572 to achieve excitation equilibrium (see text). Open circles indicate photometric temperatures obtained as described in Sect. 5.1; filled circles correspond to the adopted, excitation-equilibrium values.

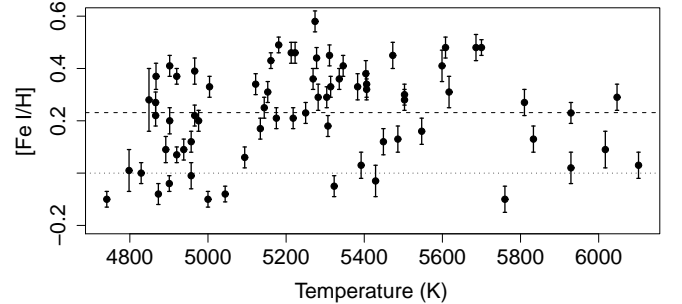


Fig. 11:  $[\text{Fe I}/\text{H}]$  vs. temperatures. Dashed and dotted lines indicate the mean iron abundance and  $[\text{Fe}/\text{H}] = 0$ , respectively.

$T_{\text{eff}}$ , parallaxes, apparent magnitudes, and  $[\text{Fe}/\text{H}]$  as input values, we recovered the possible solutions for  $\log g$ , masses, and ages, which are within the errors in  $T_{\text{eff}}$ ,  $M_V$  and  $[\text{Fe}/\text{H}]$ , and computed the mean values. This procedure was repeated 200 times, and each time, the input values were varied following a normal distribution with mean  $X$  and standard deviation of  $\sigma_X$ , where  $X$  (with  $X = T_{\text{eff}}$ ,  $M_V$  and  $[\text{Fe}/\text{H}]$ ) is the parameter value and  $\sigma_X$  is the error associated with it. The internal errors on masses and ages were then computed as the standard deviation of the output values of these 200 realizations; errors of about 3% were found.

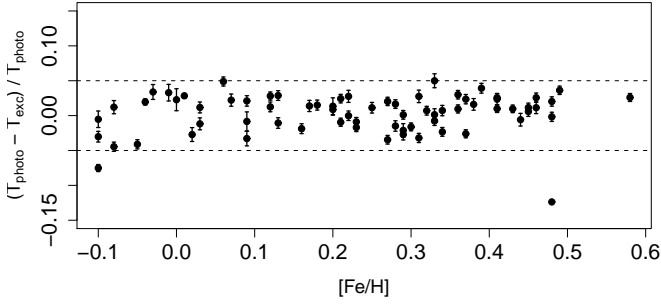


Fig. 12: Differences between photometric and excitation temperatures vs. metallicities. The dashed lines indicate  $\pm 5\%$ .

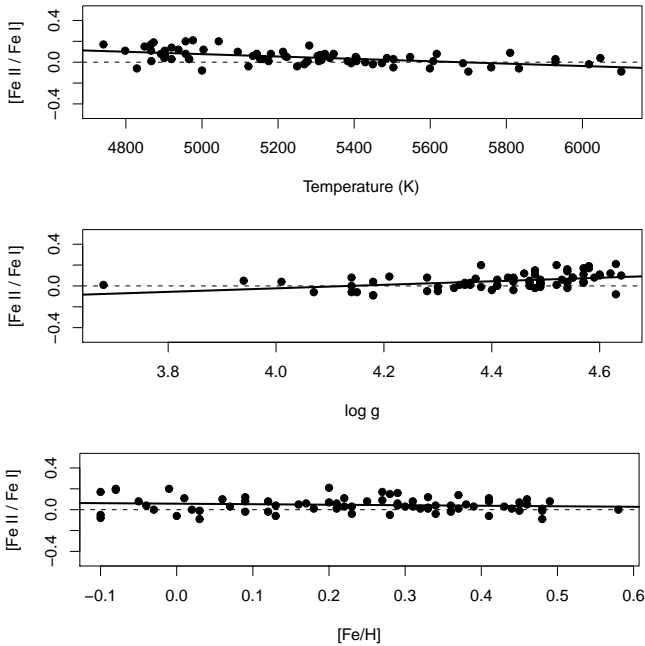


Fig. 13: Ionization equilibrium as a function of temperature (*top*), gravity (*middle*), and metallicity (*bottom*).  $[\text{Fe I}/\text{Fe II}]$  is the difference between abundances from neutral and single ionized iron lines,  $[\text{Fe I}/\text{H}] - [\text{Fe II}/\text{H}]$ .

To check the accuracy of our mass determination method, we derived the masses of stars listed in Torres et al. (2010). These authors have produced the most recent compilation of high-accuracy mass determinations in binaries ( $< 3\%$ ). We selected stars with temperatures and distances similar to those of our sample stars: parallaxes in the range 11 to 70 mas and temperatures from 4500 to 6500 K. We found 14 stars satisfying these criteria. Using the temperatures from these authors and solar metallicity, we derived the masses using the same method as was applied to our stars. We found that masses obtained with  $Y^2$  isochrones are 4% lower than masses from Torres et al., with a standard deviation of 5%. The good accuracy found in the present work comes from the narrower range of parameters considered here. Despite having found a systematic difference between masses

from isochrones and those from dynamical considerations, no corrections were applied to the masses of our sample stars, since this difference would lead to lower  $\log g$  only by an amount of  $< 0.02$  dex, and the effect in the resulting abundances would be negligible. We added these uncertainties to the internal errors of masses and  $\log g$ .

We also derived the stellar masses from the Padova (Girardi et al. 2000) isochrones with the tool PARAM (da Silva et al. 2006) (see also Sect. 5.2). We found that masses estimated from Padova isochrones are  $\sim 5\%$  lower than  $Y^2$  masses, and this difference leads to lower gravities by  $\sim 0.02$  dex.

Using the same procedure for mass determinations, we obtained the ages for all sample stars. The ages of 36 stars could be determined with errors smaller than 30%, and for 22 of them, the errors are within 20%. The stellar masses, ages, and their uncertainties for all sample stars are reported in Table 13.

### 5.6. Final parameters and comparison with other studies

The final adopted temperatures, gravities, and metallicities were compared with data available in the literature. For comparison purposes, the parameters ( $T_{\text{eff}}$ ,  $\log g$ ,  $[\text{Fe}/\text{H}]$ ) were retrieved from the PASTEL catalogue (Soubiran et al. 2010), which compiles stellar atmospheric parameters obtained from the analysis of high-resolution, high signal-to-noise spectra. We only took into account analyses more recent than the year 1997 into account, keeping only from previous year the reference paper of McWilliam (1990). The parameters of 38 of our sample stars are available in this catalogue. Table 8 presents the mean values and standard deviations (when more than one value is available) of ( $T_{\text{eff}}$ ,  $\log g$ ,  $[\text{Fe}/\text{H}]$ ). The differences are also reported. The selected list of stellar parameters given in this catalogue is reported in Table A.2.

The comparisons are presented in Fig. 14. Differences between temperatures considered in the present work and those from the PASTEL catalogue do not exceed 2%, except for two stars (HD 31827 and HD 35854). We also found good agreement between gravities, with differences within  $\sim 0.2$  dex.

The metallicities derived in this work are in good agreement with the values reported in the literature for  $[\text{Fe}/\text{H}] \lesssim 0.3$ . At higher metallicities ( $[\text{Fe}/\text{H}] \gtrsim 0.3$ ), the abundances determined in this work are systematically higher than the values reported in the literature by  $\sim 0.1$  dex on average. On the other hand, there are no systematic differences between temperatures and gravities for  $[\text{Fe}/\text{H}] \gtrsim 0.3$ ; thus, it is unlikely that differences in stellar parameters are the source of our higher metallicities.

We also compared the present final metallicities and the photometric metallicities from the GCS survey. Our sample contains 17 stars in common with GCS, and the mean difference between the metallicities of these stars is  $[\text{Fe}/\text{H}]_{\text{present}} - [\text{Fe}/\text{H}]_{\text{GCS}} = 0.08 \pm 0.12$ . Improved new calibrations of the GCS data from Casagrande et al. (2011) brings the GCS metallicity scale into agreement with ours: using the temperatures from CRM10 calibrations, Casagrande et al. also found higher  $[\text{Fe}/\text{H}]$  by an amount of 0.1 dex.

Finally, the metallicities derived from the Geneva photometry, presented in Table 13, show differences of spectroscopic iron abundances derived in the present work being  $-0.12 \pm 0.16$  dex lower than the Geneva photometric metallicities.



Table 8: Data from the PASTEL catalogue

Star	$T_{\text{eff}}$ (K)	$\Delta T_{\text{eff}}$ (K)	$\log g$	$\Delta \log g$	[Fe/H]	$\Delta[\text{Fe}/\text{H}]$
HD 8389	5330 ± 67	-56	4.44 ± 0.09	0.03	0.41 ± 0.09	0.17
HD 9424	5420 ± ...	29	...	...	...	...
HD 10576	5882 ± ...	47	...	...	...	...
HD 13386	5294 ± 95	-24	4.28 ± ...	0.26	0.26 ± ...	0.10
HD 15555	4855 ± 20	12	...	...	...	...
HD 25061	5321 ± ...	-14	...	...	...	...
HD 26151	5353 ± 22	30	4.39 ± 0.11	0.02	0.27 ± 0.01	0.06
HD 26794	4930 ± 29	-10	4.74 ± ...	-0.25	0.07 ± 0.04	0.00
HD 27894	4914 ± 54	6	4.30 ± 0.12	0.24	0.25 ± 0.07	0.12
HD 30295	5417 ± 74	-11	4.29 ± 0.30	0.07	0.22 ± 0.09	0.10
HD 31452	5262 ± ...	-12	...	...	...	...
HD 31827	5508 ± 150	100	4.12 ± 0.39	0.23	0.30 ± 0.15	0.17
HD 35854	4928 ± 32	-27	4.54 ± 0.11	0.04	-0.09 ± 0.06	0.05
HD 37986	5507 ± 66	-4	4.38 ± 0.06	0.09	0.27 ± 0.05	0.03
HD 39213	5372 ± 120	100	4.18 ± 0.25	0.20	0.28 ± 0.11	0.17
HD 39715	4816 ± 25	-75	4.75 ± ...	-0.18	-0.04 ± ...	-0.06
HD 77338	5290 ± 0	56	4.75 ± 0.21	-0.20	0.26 ± 0.06	0.15
HD 82943	6000 ± 44	-70	4.43 ± 0.08	-0.08	0.27 ± 0.04	-0.04
HD 86065	5026 ± ...	-88	4.50 ± ...	0.12	-0.06 ± ...	0.15
HD 86249	4961 ± ...	-4	...	...	...	...
HD 87007	5282 ± 29	0	4.55 ± 0.21	-0.01	0.27 ± 0.00	0.02
HD 90054	6080 ± ...	-33	...	...	...	...
HD 104212	5996 ± ...	-163	...	...	...	...
HD 107509	6069 ± ...	33	...	...	...	...
HD 120329	5636 ± ...	-19	...	...	...	...
HD 148530	5402 ± ...	-10	...	...	...	...
HD 149933	5735 ± ...	-249	...	...	...	...
HD 165920	5342 ± 5	-6	4.38 ± 0.02	0.09	0.30 ± 0.01	0.06
HD 171999	5288 ± 55	16	4.65 ± ...	-0.16	0.40 ± ...	-0.11
HD 180865	5255 ± ...	-37	...	...	...	...
HD 181234	5415 ± 121	-104	4.47 ± ...	-0.10	0.36 ± ...	0.09
HD 181433	4958 ± 6	-56	4.37 ± ...	0.20	0.33 ± ...	0.08
HD 182572	5583 ± 172	117	4.16 ± 0.17	0.02	0.38 ± 0.09	0.10
HD 197921	4948 ± ...	-82	...	...	...	...
HD 211706	6023 ± ...	-6	...	...	...	...
HD 218566	4927 ± ...	-78	4.81 ± ...	-0.33	0.38 ± ...	-0.10
HD 218750	5227 ± ...	-93	...	...	...	...
HD 224383	5751 ± 14	9	4.36 ± 0.06	-0.08	-0.06 ± 0.02	-0.04

## 6. Abundance determination

### 6.1. Carbon, oxygen, magnesium, and calcium

To derive the abundance of C, O, Mg, and Ca, we performed spectral synthesis, and the abundances were obtained by minimizing the  $\chi^2$  between the observed and synthetic spectra. The synthetic spectra were obtained using the PFANT code described in Cayrel et al. (1991), Barbuy et al. (2003), and Coelho et al. (2005) which includes molecular lines in the ABON2 code (Sect. 5.3). Again, the same MARCS model atmospheres are employed.

#### Carbon

The carbon abundances were derived from the CI 5380 Å line, adopting the line list given in Spite et al. (1989). To check the atomic parameters, we derived the solar carbon abundance by  $\chi^2$  minimization between observed and synthetic solar spectra, obtaining  $(\text{C}/\text{H})_{\odot} = 8.53$ . This value is in good agreement with abundances from Grevesse et al. (1996),  $(\text{C}/\text{H})_{\odot} = 8.55$ , and Grevesse & Sauval (1998),  $(\text{C}/\text{H})_{\odot} = 8.52$ .

Table 9: Nickel blend at 6300 Å.

Species	$\lambda$ (Å)	$\chi_{\text{exc}}$ (eV)	$\log gf$
Ni I	6300.335	4.27	-2.275
Ni I	6300.355	4.27	-2.695
[O I]	6300.340	0.00	-9.820

#### Oxygen

The oxygen abundances were determined using the forbidden line at 6300 Å. The blend with nickel was taken into account using the atomic data from Bensby et al. (2004) (Table 9). Since previous studies suggest that the [Ni/Fe] ratio increases at higher metallicities (Bensby et al. 2005), the contribution of the Ni blend at 6300 Å may be important for our sample stars. For this reason, the abundances of Ni were previously derived, in order to consider the correct ratio [Ni/Fe] for each star.

To check the atomic parameters, we derived the solar oxygen abundance, obtaining  $(\text{O}/\text{H})_{\odot} = 8.63$ . This value is in good agreement with  $(\text{O}/\text{H})_{\odot} = 8.66$  from Asplund et al. (2005).

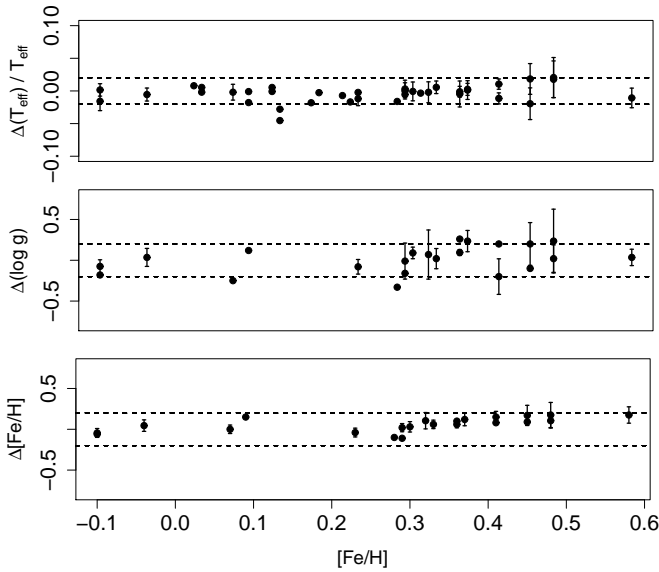


Fig. 14: Relative differences between temperatures (*top*), gravities (*middle*), and metallicities (*bottom*) derived in the present work and from the PASTEL catalogue. Differences are *this work* - PASTEL. Dashed lines indicate  $\pm 2\%$  in the  $T_{\text{eff}}$  panel and  $\pm 0.2$  dex in the  $\log g$  and metallicity panels.

## Magnesium

The magnesium abundances were obtained using the triplet Mg I lines at 6319 Å. A Ca I line at 6318.3 Å showing autoionization effects, producing a  $\sim 5$  Å broad line, can affect the determination of the continuum placement (e.g. Lecureur et al. 2007). The Ca I autoionization line was treated by increasing its radiative broadening to reflect the much reduced lifetime of the level suffering autoionization compared with the radiative lifetime of this level. The radiative broadening had to be increased by 16 000 of its standard value ( $\propto 1/\lambda^2$ , based on the radiative lifetimes alone) to reproduce the Ca I dip in the solar spectrum (Fig. 15). In addition, the abundances of Ca of each star were derived before the calculations of the synthetic spectra at the 6319 Å region, in order to take the correct [Ca/Fe] ratio into account in the computation of the Ca line. Even if the majority of the stars in the sample are not affected, since their abundance ratios are close to solar ([Ca/Fe]  $\sim 0.00$ ), for some of the sample stars the effect can be important. Figure 16 presents the spectrum of HD 201237 at the 6319 Å region. The contribution of the Ca I autoionization line is shown considering both [Ca/Fe] = 0.00 and [Ca/Fe] = 0.37. The latter is the abundance ratio of HD 201237 before the correction of the trend with temperature (Sect. 6.3). It is clear that the Ca abundance of this star must be taken into account to reproduce the Ca I dip. The resulting differences in the Mg abundance considering solar and non-solar [Ca/Fe] ratio are  $\sim 0.07$  dex in average.

To check the atomic parameters of the lines at the Mg I triplet region (Table 10), we derived the solar Mg abundance. We obtained  $(\text{Mg}/\text{H})_{\odot} = 7.60$ , in good agreement with  $(\text{Mg}/\text{H})_{\odot} = 7.58$  from Grevesse & Sauval (1998).

Sun – Mg  $\lambda 6319$  Å

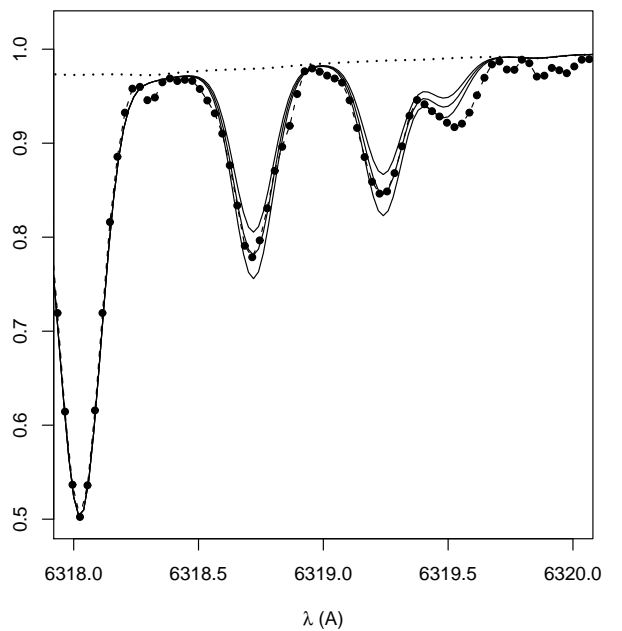


Fig. 15: Solar spectra in the region of the 6319 Å Mg triplet. Solid lines indicate the synthetic spectra for  $(\text{Mg}/\text{H}) = 7.50, 7.60, 7.70$ ; the dots indicate the observed spectrum. The dotted line shows the contribution of the Ca I autoionization line.

## Calcium

The Ca I lines were selected from Bensby et al. (2004), Spite et al. (1987), and Barbuy et al. (2009), and they are listed in Table A.3. The  $\log gf$  values were fitted to the solar line profiles, using  $(\text{Ca}/\text{H})_{\odot} = 6.36$  (Grevesse & Sauval 1998). The lines that give unreliable abundances were identified using the same procedure as applied to Fe lines, and the differences  $A_{\lambda i} - \langle A \rangle_i$  for all the sample stars are plotted in Fig. 17.

## 6.2. Silicon, titanium and nickel

Silicon, titanium, and nickel abundances were determined by recovering the measured equivalent widths through LTE analysis with the ABON2 code (Spite 1967). Again, the equivalent widths were measured with the ARES code, and errors in  $W_{\lambda}$  were estimated by carrying out the same procedure as described in Sect. 5.3. Ti, Si, and Ni spectral lines were selected from Bensby et al. (2004), Cohen et al. (2009), and Pompéia et al. (2007). Through a similar procedure used in the iron abundance determination, the  $\log gf$  values were fitted to the solar equivalent widths, adopting  $(\text{Ti}/\text{H})_{\odot} = 5.02$ ,  $(\text{Si}/\text{H})_{\odot} = 7.55$  and  $(\text{Ni}/\text{H})_{\odot} = 6.25$  (Grevesse & Sauval 1998). The final line list and the astrophysical  $\log gf$  values are presented in Table A.3.

Lines that give unreliable abundances were identified with the same procedure as used for iron lines. We computed the differences between the abundance of each star,  $\langle A \rangle_i$ , and the abundance derived from an individual line,  $A_{\lambda i}$ . The differences  $A_{\lambda i} - \langle A \rangle_i$  for all sample stars are plotted in Fig. 17.

Table 10: Lines at the 6319 Å region.

Species	$\lambda$ (Å)	$\chi_{ex}$ (eV)	$\log gf$ (Sun)	$\log gf$ (NIST)	$\log gf$ (VALD)	$\log gf$ (BZO+09)
Fe I	6318.03	2.45	-1.80	-1.80	-2.26	...
Ti I	6318.03	1.43	-0.94	...	...	...
Ca I	6318.35	4.43	0.06	...	0.06	...
Mg I	6318.72	5.11	-1.98	-2.10	-1.73	-2.10
Mg I	6319.24	5.11	-2.23	-2.32	-1.95	-2.36
Mg I	6319.49	5.11	-2.80	-2.80	-2.43	-2.80

Notes. BZO+09: Barbuy et al. (2009)

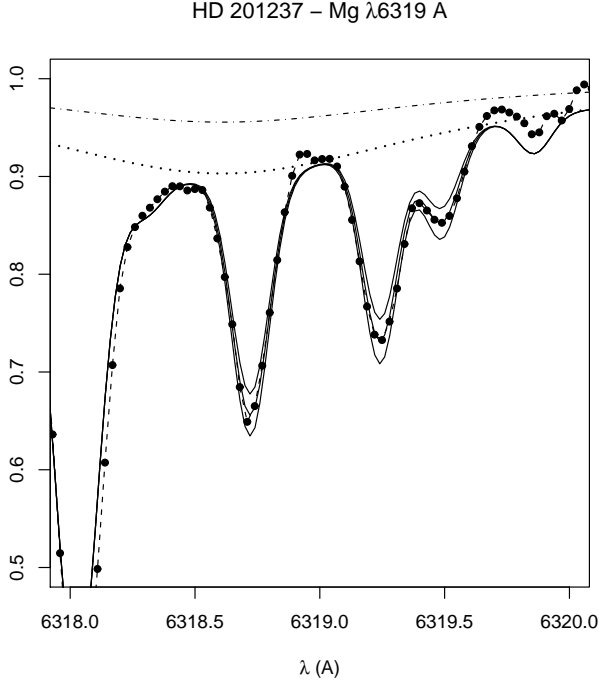


Fig. 16: Spectrum of HD 201237 in the region of the 6319 Å Mg triplet. Solid lines indicate the synthetic spectra for  $(\text{Mg}/\text{H}) = 7.53, 7.63,$  and  $7.73$ ; the dots indicate the observed spectrum. We considered the calcium abundance of HD 201237 to calculate the synthetic spectrum, and the contribution of the Ca I autoionization line is represented by the dotted curve. The dot-dashed line indicates the Ca I dip when we consider  $[\text{Ca}/\text{Fe}] = 0.00$ .

### 6.3. Spurious abundance trends and errors

Trends with effective temperature were found in previous studies. In an analysis of 1040 F, G, and K dwarf stars, Valenti & Fischer (2005) find that the abundances of Na, Si, Ti, Ni, and Fe present trends with the temperature of the star. Neves et al. (2009) derived the chemical abundances of 12 elements for a sample of 451 stars of the HARPS GTO planet search programme, and similar trends with temperatures were found.

To check such trends in our results, we plotted our final abundances against temperatures. Figure 18 shows the abundances vs.  $T_{\text{eff}}$ , and a significant trend is observed for C, Ca, and Ti abundances. Following a procedure similar to the one adopted

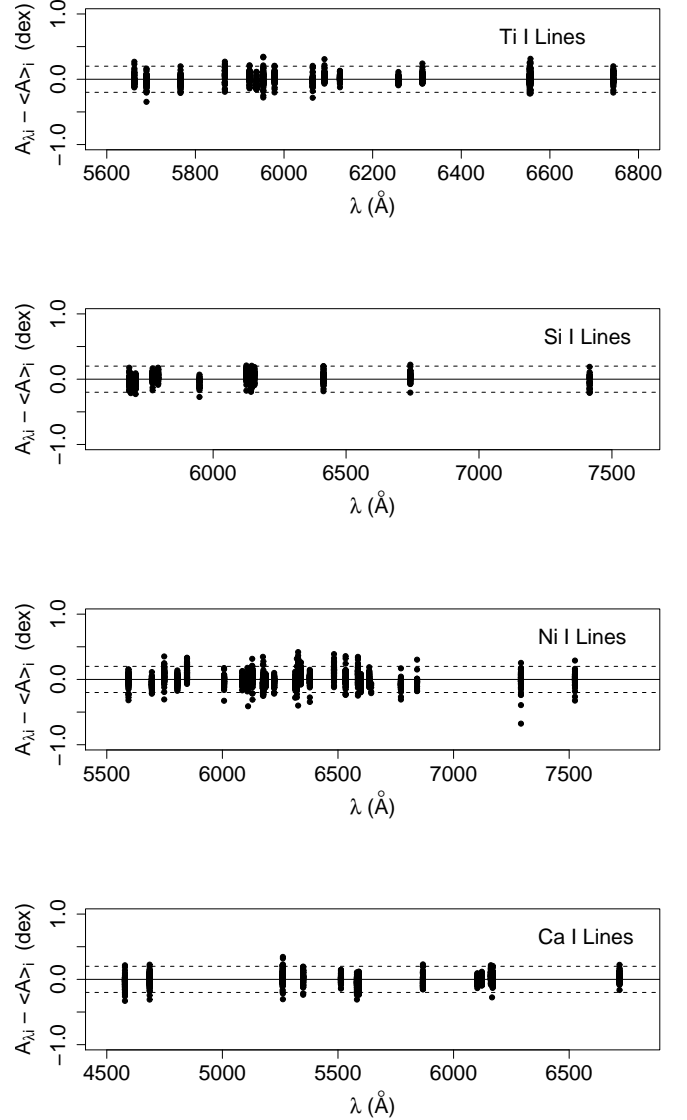


Fig. 17: Process of selection of stable lines of Ti I, Si I, and Ca I. The dashed lines indicate  $\pm 0.2$  dex.

by Valenti & Fischer (2005) and Meléndez & Cohen (2009), we corrected this trend by fitting a second-order polynomial and applied the correction for C, Ca, and Ti (Fig. 19). We assumed that abundance trend corrections are zero at  $T_{\text{eff}} = 5777$  K. This as-

sumption eliminates the possibility that the Sun itself may have peculiar abundances (e.g. Allende Prieto et al. 2004).

The errors on abundances were estimated as follows. The errors on abundances of C, O, and Mg were derived by taking the uncertainties on the stellar parameters into account. Temperatures, gravities, and metallicities were varied individually according to their errors, and the resulting variations on the abundance were added quadratically. This procedure were performed for ten stars in the sample, and the mean error was assumed to be the characteristic error for the sample stars (0.12, 0.17, and 0.08 dex for C, O, and Mg, respectively). More than one spectral line was used to derive the abundances of Ni, Si, Ca, and Ti, and for these elements, the errors are assumed to be the standard deviation of the abundances derived from individual lines. The errors on these four abundances are presented in Tables 14 and 15.

#### 6.4. Final abundances and comparison with other studies

To test the reliability of our results, we compared the abundances derived in the present work and derivations from previous studies of Valenti & Fischer (2005) and Neves et al. (2009). Our sample contains 12 stars in common with the sample studied by Valenti & Fischer and eight in common with Neves et al. In Table 11, we give the mean difference between the abundance ratios  $[X/Fe]$ , and in Fig. 20, these differences are shown as a function of  $[Fe/H]$ . Our results are in good agreement with the abundances derived by these authors. Differences are all within  $\sim 0.2$  dex, and there is no evident trend with metallicity.

The final abundances relative to iron,  $[X/Fe]$ , vs.  $[Fe/H]$  are presented in Fig. 21. We plotted the abundances from Bensby et al. (2003), Bensby et al. (2004) and Mishenina et al. (2004, 2008), and Reddy et al. (2003, 2006) for a comparison. We applied the same procedure as described in Sect. 4.2 to separate the samples of these studies into thin disk, thick disk, and intermediate populations<sup>4</sup>. We stress that the comparison must be considered carefully: different approaches and methods can lead to systematic differences between abundances from different authors. These systematic differences could be determined by direct comparison of abundances for stars in common with other samples. However, our sample contains only two stars in common with the sample of Bensby et al. (2004) and one in common with Mishenina et al. (2004, 2008), so that the systematic differences could not be quantified accurately. By comparing the abundances of these stars (even if they are so few), we found that our results are 0.04 dex lower than  $[\alpha/Fe]$  ratios from these studies. Differences at this level do not affect the main conclusions of this work.

We found the following trends of  $[X/Fe]$  vs.  $[Fe/H]$  for each element:

*Carbon:*  $[C/Fe]$  is a decreasing function of metallicity. The median value of  $[C/Fe]$  at lower metallicities ( $[Fe/H] < 0.2$ ) is 0.03, while we found  $[C/Fe] - 0.07$  for the more metal-rich stars ( $[Fe/H] > 0.2$ ).

*Oxygen:*  $[O/Fe]$  decreases with increasing metallicity. Eight stars with metallicity  $0.2 < [Fe/H] < 0.4$  have  $[O/Fe] \approx 0.2$ . Among these, five are assigned to the thick disk, two to the

<sup>4</sup> To perform a consistent comparison, we re-classified the samples from these authors, using the same procedure as for our sample. Hereafter, the thin disk, the thick disk, and intermediate populations from Bensby et al. (2003, 2004), Mishenina et al. (2004, 2008), and Reddy et al. (2003, 2006) refer to the classification described in Sect. 4.2.

intermediate population, and one to the thin disk. This overabundance is within the errors; therefore higher S/N spectra would be interesting to verify their oxygen abundances with higher precision, since these could be a distinct category of stars, but there is no evidence for such a conclusion with the present data.

*Nickel:* The nickel-to-iron ratio is constant up to  $[Fe/H] \sim 0.2$ , and increases at higher metallicities. This trend has already been suggested by data from Bensby et al. (2004), and is confirmed here.

*Magnesium, silicon, calcium, and titanium:* The abundance of these elements present a low scatter and follows the general trend of thin disk stars.

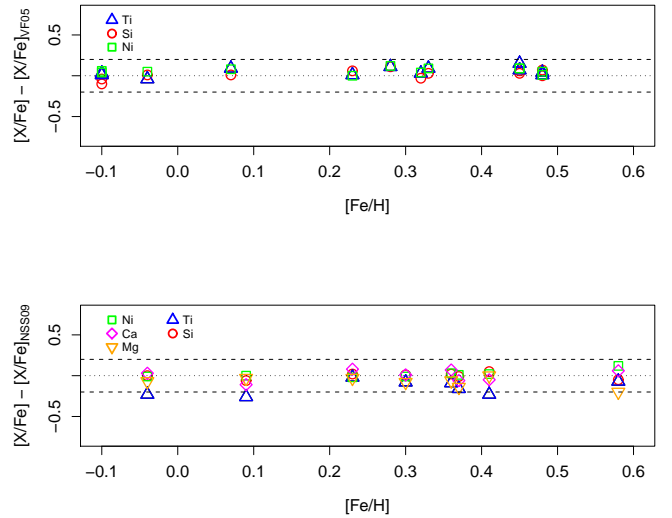


Fig. 20: Comparison of abundances with other studies. The upper panel shows differences between our abundances of Si, Ti, and Ni and those from Valenti & Fischer (2005). The bottom panel presents the comparisons of Si, Ti, Ca, Mg, and Ni abundances from Neves et al. (2009).

## 7. Discussion

In the present work we concentrate efforts on studying metal-rich stars with  $[Fe/H] > 0.0$ , from a sample of high proper-motion, NLTT-selected stars as described in Sect. 2. In Pompéia et al. (2003), we studied the behaviour of  $[\alpha/Fe]$  as a function of metallicity in the range  $-0.8 < [Fe/H] < +0.4$ , for stars with similar kinematics to the present sample. It was found that the enhancement of  $\alpha$ -elements relative to Fe drops with increasing metallicity, reaching solar ratios at around  $[Fe/H] \approx -0.4$  for Si, Ca, and Ti, and at  $[Fe/H] \approx -0.2$  for Mg and O. This behaviour is compatible with the thick disk characteristics. Bensby et al. (2003) shows a drop in  $[\alpha/Fe]$  at  $[Fe/H] \approx -0.4$ , reaching the solar ratio at  $[Fe/H] \approx 0.0$ . It was shown in Sect. 6 that  $\alpha$ -element abundances are not enhanced in the metal-rich sample stars, a result compatible with the behaviour previously shown by Pompéia et al. (2003).

In terms of kinematical properties, we analysed the U, V, W velocities of the sample stars to identify members of the thick



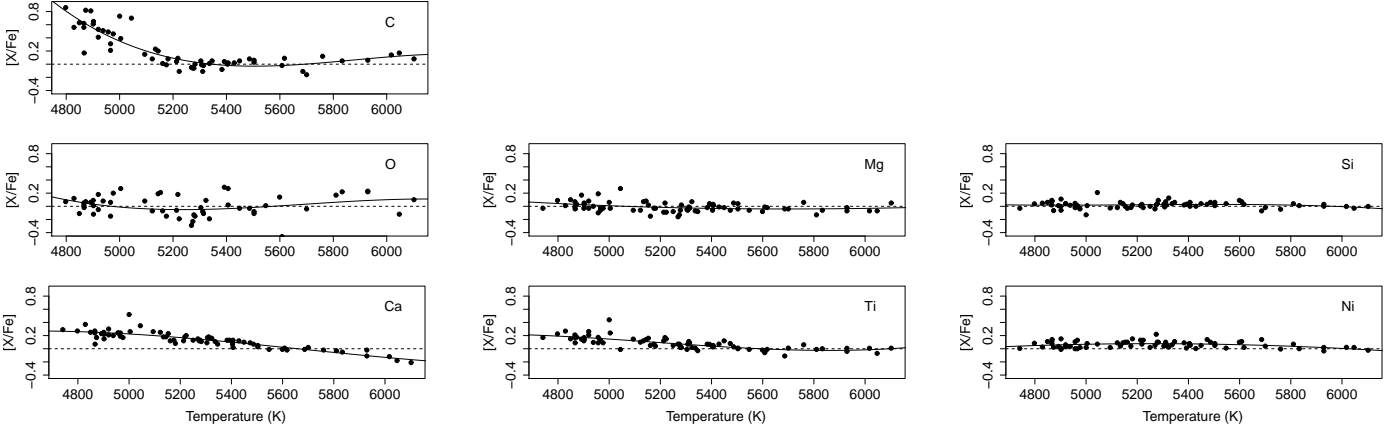


Fig. 18: Abundances of C, O, Mg, Si, Ca, Ti, and Ni vs. temperature. A pronounced trend is observed for C, Ca and Ti.

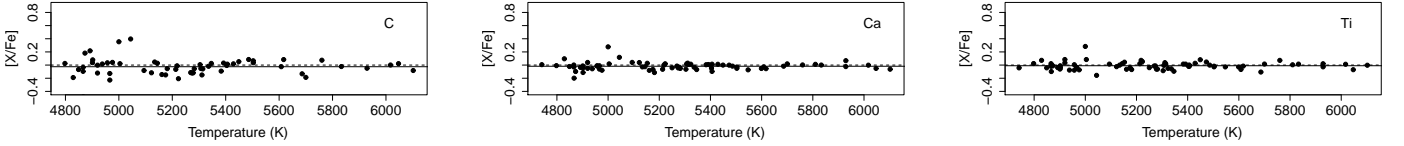


Fig. 19: Abundances of C, Ca, and Ti vs. temperature after the correction. We considered the mean abundance in the range  $5680 < T_{\text{eff}} < 5880$  K as the zero point of the correction, which is  $-0.03$ ,  $-0.02$ , and  $-0.01$  for C, Ca, and Ti, respectively.

Table 11: Comparison of abundances with other studies

Reference	$\Delta[\text{Fe}/\text{H}]$	$\Delta[\text{Ca}/\text{Fe}]$	$\Delta[\text{Mg}/\text{Fe}]$	$\Delta[\text{Si}/\text{Fe}]$	$\Delta[\text{Ti}/\text{Fe}]$	$\Delta[\text{Ni}/\text{Fe}]$	#
Valenti & Fischer (2005)	$0.01 \pm 0.07$	...	...	$0.02 \pm 0.06$	$0.05 \pm 0.05$	$0.06 \pm 0.04$	12
Neves et al. (2009)	$0.10 \pm 0.08$	$0.12 \pm 0.11$	$0.04 \pm 0.07$	$0.00 \pm 0.04$	$-0.14 \pm 0.09$	$0.02 \pm 0.04$	8

**Notes.**  $\Delta[\text{X}/\text{Fe}] = \langle [\text{X}/\text{Fe}]_{\text{Our}} - [\text{X}/\text{Fe}]_{\text{Other}} \rangle$

disk, thin disk and intermediate ones, according to definitions by Soubiran et al. (2003). The membership with thin or thick disk components discussed in Sect. 4.2 leads to 42 (59%) of the sample stars to be identified with the thick disk.

### 7.1. Comparison with thin and thick disk stars

We compared the characteristics of the sample stars with thin disk, thick disk, and intermediate populations from Bensby et al. (2003, 2004), Mishenina et al. (2004, 2008), and Reddy et al. (2006).

The sample is dominated by stars having the metallicities indicative of thin disk population, as seen by the behaviour of  $[\alpha\text{-elements}/\text{Fe}]$  vs.  $[\text{Fe}/\text{H}]$  presented in Fig. 21. On the other hand, the kinematics of the sample stars would suggest membership with the thick disk, as shown in the UV plane and Toomre diagram (Fig. 22). If confirmed as members of the thick disk, these metal-rich stars provide an interesting sample for testing models of thick disk formation. They show the kinematics of a thick disk, together with the metallicities and abundance ratios of thin disk stars.

In Fig. 23, we show the space velocities U, V, and W against  $[\alpha/\text{Fe}]$ . The sample stars show a lower rotational velocity V than the thin disk stars. The |W| velocity is somewhat higher than

the thin disk, showing essentially only negative values, which may be further investigated in terms of migration effects in the Galaxy.

Grenon (1987) proposed that the average radius of the orbit,  $R_m = (R_{\text{max}} + R_{\text{min}})/2$ , is kept close to the initial galactocentric radius of the stellar birthplace. Therefore, we are able to use  $R_m$  to derive radial constraints, such as the abundance gradients for each population. Figure 27 shows how the metallicity and  $[\alpha/\text{Fe}]$  vary with respect to  $R_m$  for thin, thick, and intermediate stars. The thin and thick disk stars appear to have  $R_m \sim 8$  and 6 kpc, whereas the intermediate population has  $R_m \sim 7$  kpc. These distances agree with  $R_m$  distances of our thin disk, thick disk, and intermediate subsamples. Therefore, we investigate whether  $R_m$  for each component remains the same when considering the more complete sample from GCS. This is shown in Fig. 28, and it is clear that the GCS data also show that thin, thick, and intermediate stars have these typical  $R_m$  values.

Figure 24 shows  $[\text{Fe}/\text{H}]$  and  $[\alpha/\text{Fe}]$  vs. the stellar ages. The ages of the sample stars span from  $\sim 2$  to  $\sim 14$  Gyr, with mean age of 7 to 8 Gyr. In this plot, the large symbols represent stars for which ages could be determined with uncertainties lower than 30%, and the remaining stars are shown as small symbols. The older stars in the sample present lower metallicities and higher  $\alpha$ -element enhancement. To verify if different

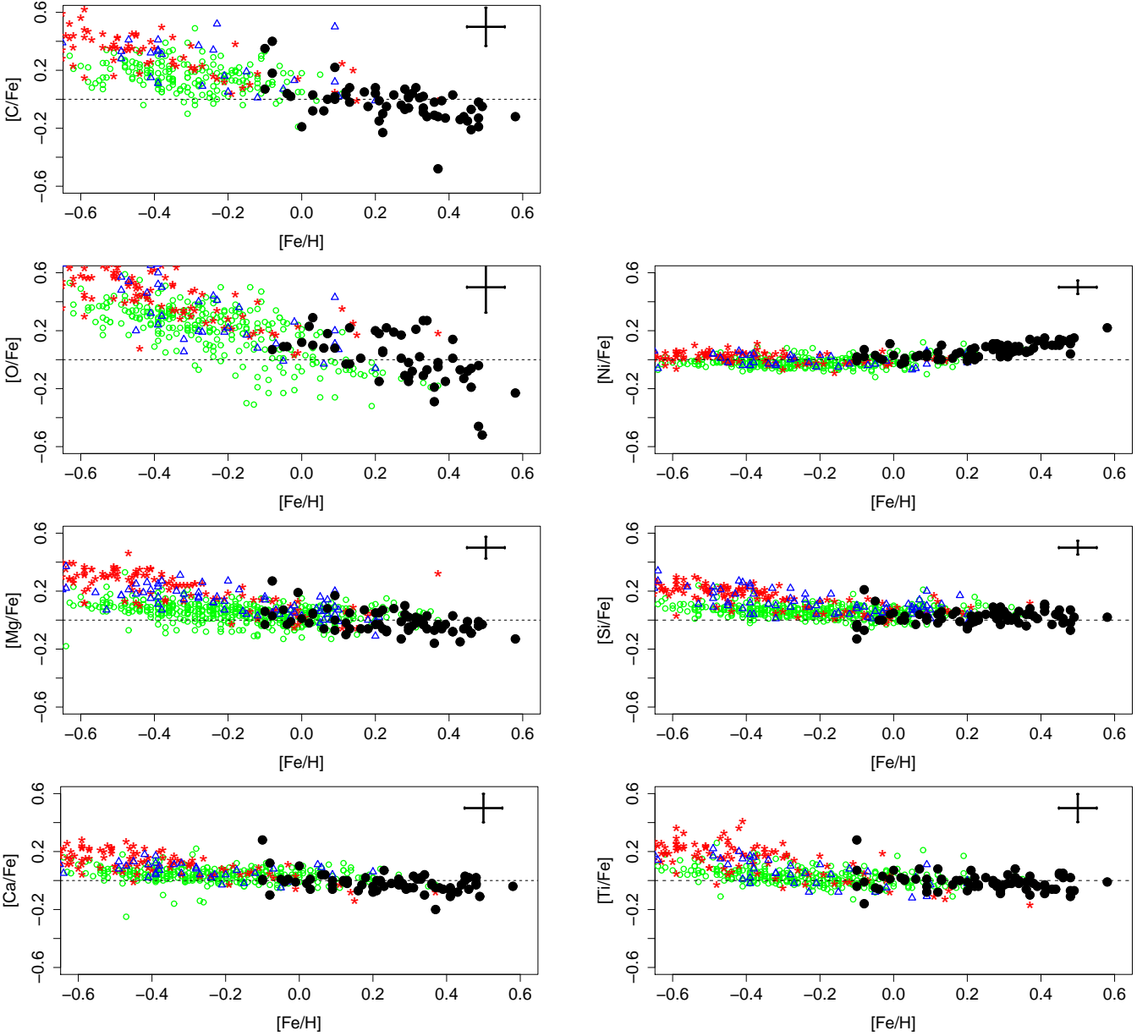


Fig. 21: Abundances of C, O, Ni, Mg, Ca, Si, and Ti vs. metallicities. The abundances derived in this work (black circles) are compared with the thin (green circles), thick (red stars) disk stars, and the intermediate population (blue triangles) from Bensby et al. (2003, 2004), Mishenina et al. (2004, 2008), and Reddy et al. (2003, 2006).

ages,  $[\text{Fe}/\text{H}]$  and  $[\alpha/\text{Fe}]$  correspond to different populations, in Figure 25 we show the same as Fig. 24 for each subsample. Thin disk, thick disk, and intermediate populations are indicated by different symbols. It seems that the three subsamples span the same range of ages, and the trends of decreasing metallicity with increasing age and increasing  $[\alpha/\text{Fe}]$  with increasing age are observed for both thin and thick disk stars. Therefore, the evolution of abundances appear to be very similar for the three populations.

The maximum height from the Galactic plane  $Z_{\text{max}}$  of our selected 42 thick disk stars, of  $Z_{\text{max}} = 380$  pc (Table 4), could be considered to be lower than a mean thick-disk height (e.g. Ivezić et al. 2008).

## 7.2. Comparison with bulge stars

Very metal-rich stars can be found in the Galactic bulge. In the most extensive high-resolution spectroscopic survey available so far, Zoccali et al. (2008) studied stars in three different fields along the Galactic minor axis and find that in the most central region of their bulge sample ( $b = -4^\circ$ ),  $\sim 30\%$  of the stars have  $[\text{Fe}/\text{H}] > 0.2$ , and more than 50% have  $[\text{Fe}/\text{H}] > 0.0$ . The fraction of very metal-rich stars decreases with increasing Galactic latitudes. We investigate the similarity between the stars studied in this work and bulge stars.

Gonzalez et al. (2011) determined the abundances of the  $\alpha$  elements Mg, Si, Ca, and Ti, and obtained a mean  $[\alpha/\text{Fe}]$  ratio of bulge stars. At solar metallicities, the bulge stars are Mg-Si-

Ca-Ti-enhanced by  $\sim 0.1$  dex at the solar metallicity, when compared with our sample stars. However, the bulge stars are giants, and the present sample consists of dwarfs, therefore systematic effects of model atmospheres and other differences are expected on the abundance analysis.

Another interesting piece of information comes from the observation of microlensed dwarf and subgiant stars. In Fig. 26 we show the abundances of O, Ni, Mg, Ca, Si, and Ti for 26 such stars, presented by Bensby et al. (2011), and we plot the abundances of our sample stars for comparison. Except for an enhanced Mg in a few of the microlensed dwarfs, the results for their six metal-rich stars are also compatible with the present results, therefore our metal-rich thick-disk star subsample could be identified with a bulge origin as well.

### 7.3. Theoretical predictions

The kinematical and chemical characteristics of the sample stars might be explained by models of radial migration of stars. Fux (1997) and Raboud et al. (1998) identified “hot” orbits produced by effects of the bar, moving stars between regions inside the bar, and outside corotation. Raboud et al. (1998) found that the old disk stars in their large sample appeared to show a positive mean U motion, with an imbalance between positive and negative U velocities reaching up to  $50 \text{ km s}^{-1}$ . A U anomaly of  $+29 \pm 2 \text{ km s}^{-1}$  with respect to the Sun and  $+19 \pm 9 \text{ km s}^{-1}$  with respect to the Galactic centre was identified. Raboud et al. suggest that the metal-rich stars within this sample appeared to wander from inside the bar, reaching the solar neighbourhood. Therefore, the kinematical anomaly for the old disk (see Sect. 2) detected by Raboud et al. could be a signature of the bar. More recently, Sellwood & Binney (2002) have shown that the transient spiral arms have a dominant effect on radial migration. If these mechanisms prove to be the origin of our thick disk sample stars, it could be that these stars are bulge or inner thick disk stars reaching the solar neighbourhood.

In recent years, radial migration has been the subject of several studies, such as Haywood (2008), Minchev & Famaey (2010), Schönrich & Binney (2009a,b), and Brunetti et al. (2010), among others. For example, Schönrich & Binney (2009b) predict that there are old very metal-rich stars in the solar neighbourhood, at a relatively low rotational velocity. In this case as well, these metal-rich stars would have an origin in the inner Galaxy.

Our subsample of 42 stars with kinematics of thick disk and solar  $\alpha$ -to-Fe ratios seems to be similar to a sample identified by Haywood (2008): his identified subsample, shown as diamonds in his Fig. 12, has kinematics of thick disk,  $[\alpha/\text{Fe}] < +0.1$ , and they are old with ages in the range 8-12 Gyr, ages characteristic of an old thin disk. Haywood (2008) assigns a status of transition objects between the two disks, but closer to an old thin disk. Despite the higher metallicity of our 42 such stars, they seem otherwise to be identical. It therefore seems that this subsample should be an inner disk, closer to the Galactic centre than Haywood’s subsample, an old thin disk component.

Indeed, radial migration from the inner disk (or bulge?) is the most probable origin of these stars. A need for more substantial radial mixing as first discussed in Wielen et al. (1996), was shown by Sellwood & Binney (2002) to be possible through the passage of recurrent transient spiral patterns. Lépine et al. (2003) and Roškar et al. (2011) present calculations demonstrating that resonant scattering with spiral arms trigger efficient migration of stars from regions at  $R \sim 4\text{-}5 \text{ kpc}$  into the solar system

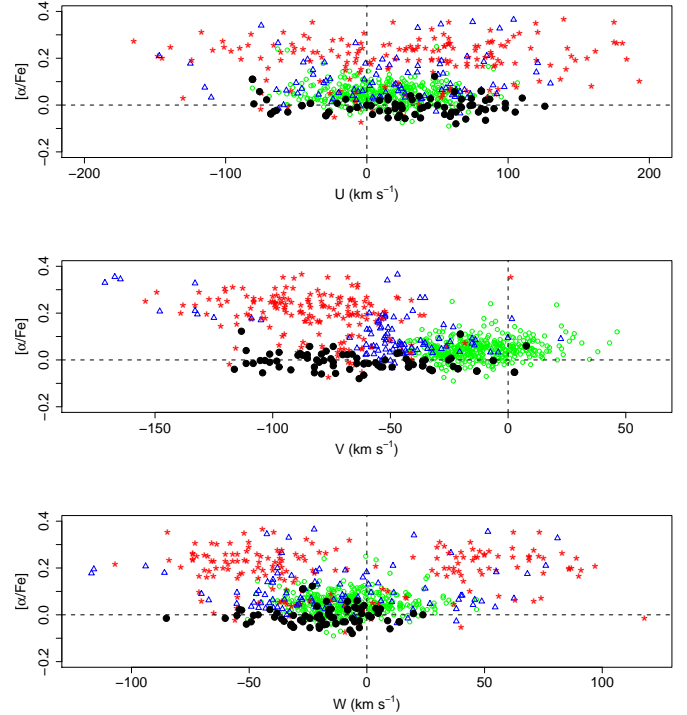


Fig. 23: UVW vs.  $[\alpha/\text{Fe}]$ . The black circles show the present sample. Data from Reddy et al. (2003, 2006); Mishenina et al. (2004, 2008); Bensby et al. (2004) are shown as red stars (thick disk), open green circles (thin disk), and blue triangles (intermediate population).

region. Roskar et al. (2011) conclude that 50% of stars in the solar neighbourhood have come from  $R < 6 \text{ kpc}$ .

Radial migration of stars could be caused by spiral and/or bar resonance. Minchev & Famaey (2010) studied the combined effect of a central bar and spiral structure on the dynamics of a galactic disk, and they find that the spiral-bar resonance overlap induces a nonlinear response leading to a strong redistribution of angular momentum in the disk. They show that a large population of stars from the bar’s corotation resonance ( $r \sim 4.5 \text{ kpc}$ ) enters the solar circle (their Fig. 6).

## 8. Summary and conclusions

In the present work, we analysed 71 metal-rich dwarf and turn-off stars, most of them old, selected from the high proper motion NLTT catalogue, as described in Raboud et al. (1998) (see Sect. 2). The aim of this work is to better understand these stellar populations, as well as to verify their high metallicities.

To be confident about the high-metallicity values, we compared the calculations carried out with two codes, from the Meudon (ABON2 code, Spite 1967) and the Uppsala (BSYN/EQWI code, Edvardsson et al. 1993) groups, and the results are similar within  $[\text{Fe}/\text{H}] \pm 0.02$ . The metallicities derived are in the range  $-0.10 < [\text{Fe I}/\text{H}] < +0.58$  from Fe I, and  $-0.18 < [\text{Fe II}/\text{H}] < +0.56$  from Fe II.

The present sample was studied by means of their kinematics and abundances. Our sample of 71 metal-rich stars can be kinematically subclassified in samples of thick disk, thin disk, and intermediate stellar populations, with mean ages of about  $7.8 \pm 3.5$ ,  $7.5 \pm 3.1$ , and  $6.8 \pm 2.9$  Gyr, respectively. It seems def-

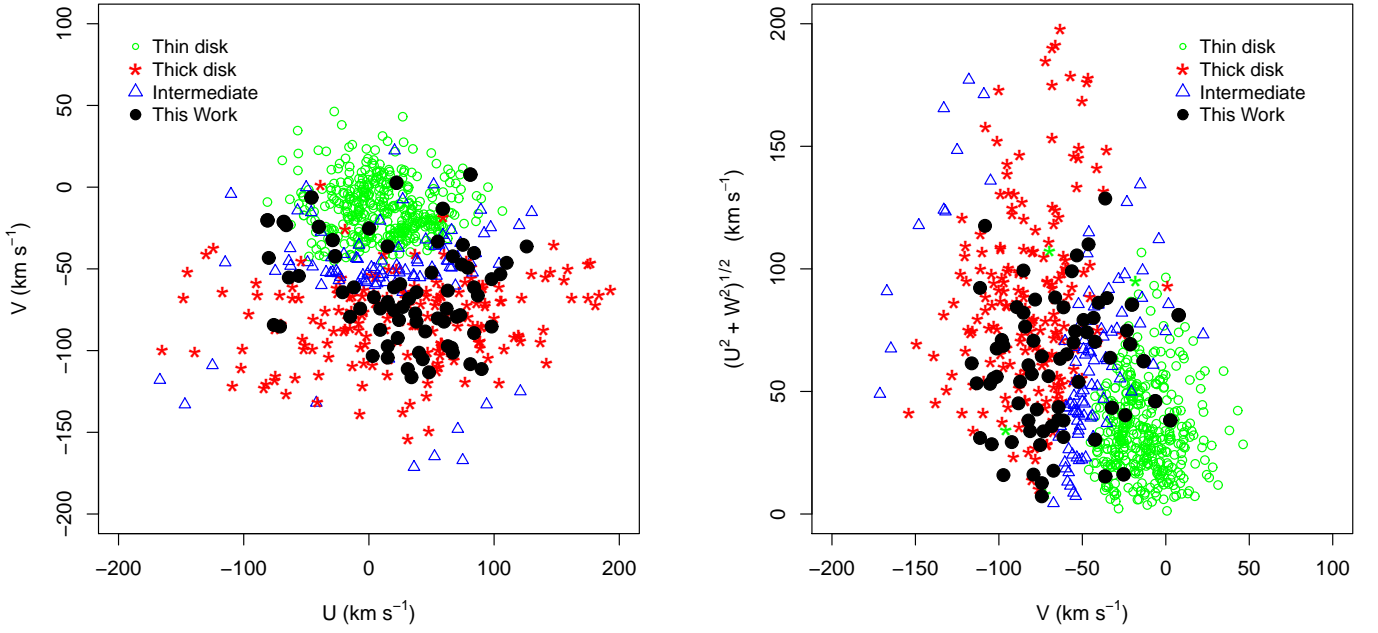


Fig. 22: *Left*: UV plane. *Right*: Toomre diagram. In both panels, the present sample is indicated by black circles. The blue open circles and red stars are the thin and thick disks, respectively. The stars shown are the samples from Reddy et al. (2003, 2006), Mishenina et al. (2004, 2008), and Bensby et al. (2004). The velocities and population fractions used (Eqs. 1 and 2) were taken from Soubiran et al. (2003).

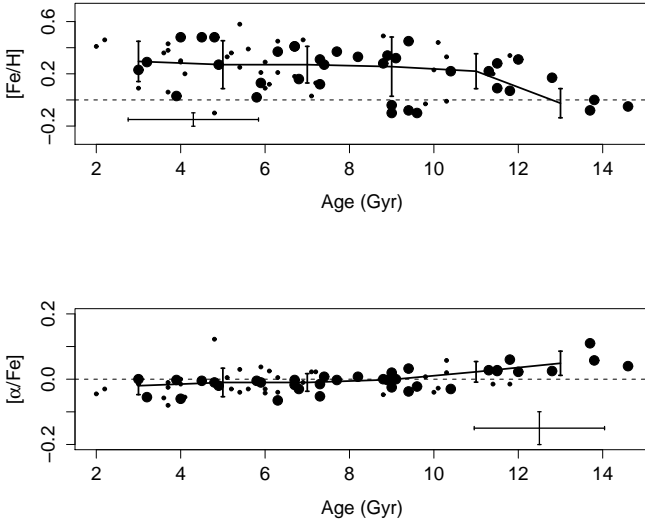


Fig. 24: Ages vs.  $[\text{Fe}/\text{H}]$  (*top*) and  $[\alpha/\text{Fe}]$  (*bottom*). The solid lines indicate the median value of  $[\text{Fe}/\text{H}]$  and  $[\alpha/\text{Fe}]$  in bins of 2 Gyr. Small symbols represent stars with age errors greater than 30%.

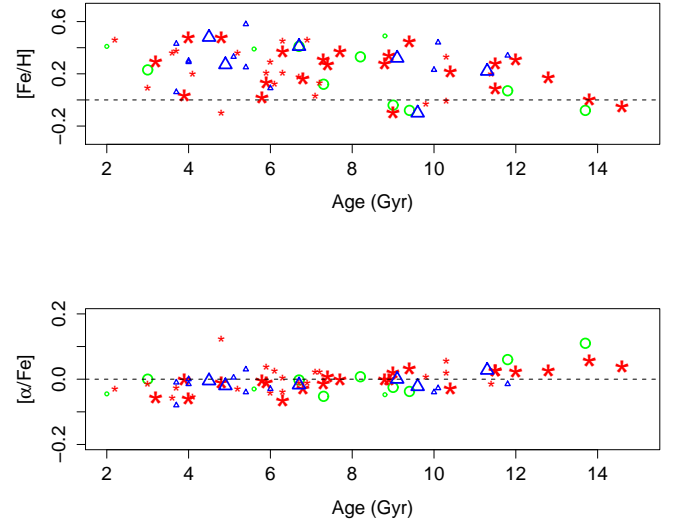


Fig. 25: Ages vs.  $[\text{Fe}/\text{H}]$  (*top*) and  $[\alpha/\text{Fe}]$  (*bottom*). Stars belonging to thin disk, thick disk, and intermediate populations are indicated as green circles, red stars, and blue triangles, respectively. Small symbols represent stars with age errors greater than 30%.

initely clear that some of the sample stars are quite old, and still quite metal rich. A most interesting feature of the sample stars is that 42 of them can be identified as belonging to the thick disk. In particular, 70% of the sample stars have space velocity  $V < -50 \text{ km s}^{-1}$ , which is more typical of a thick disk, but show

solar  $\alpha$ -to-iron ratios that are more compatible with thin disk members. This subsample appears similar to one identified by Haywood (2008), having kinematics of thick disk, together with  $[\alpha/\text{Fe}] < +0.1$ , and old ages in the range 8-12 Gyr; Haywood



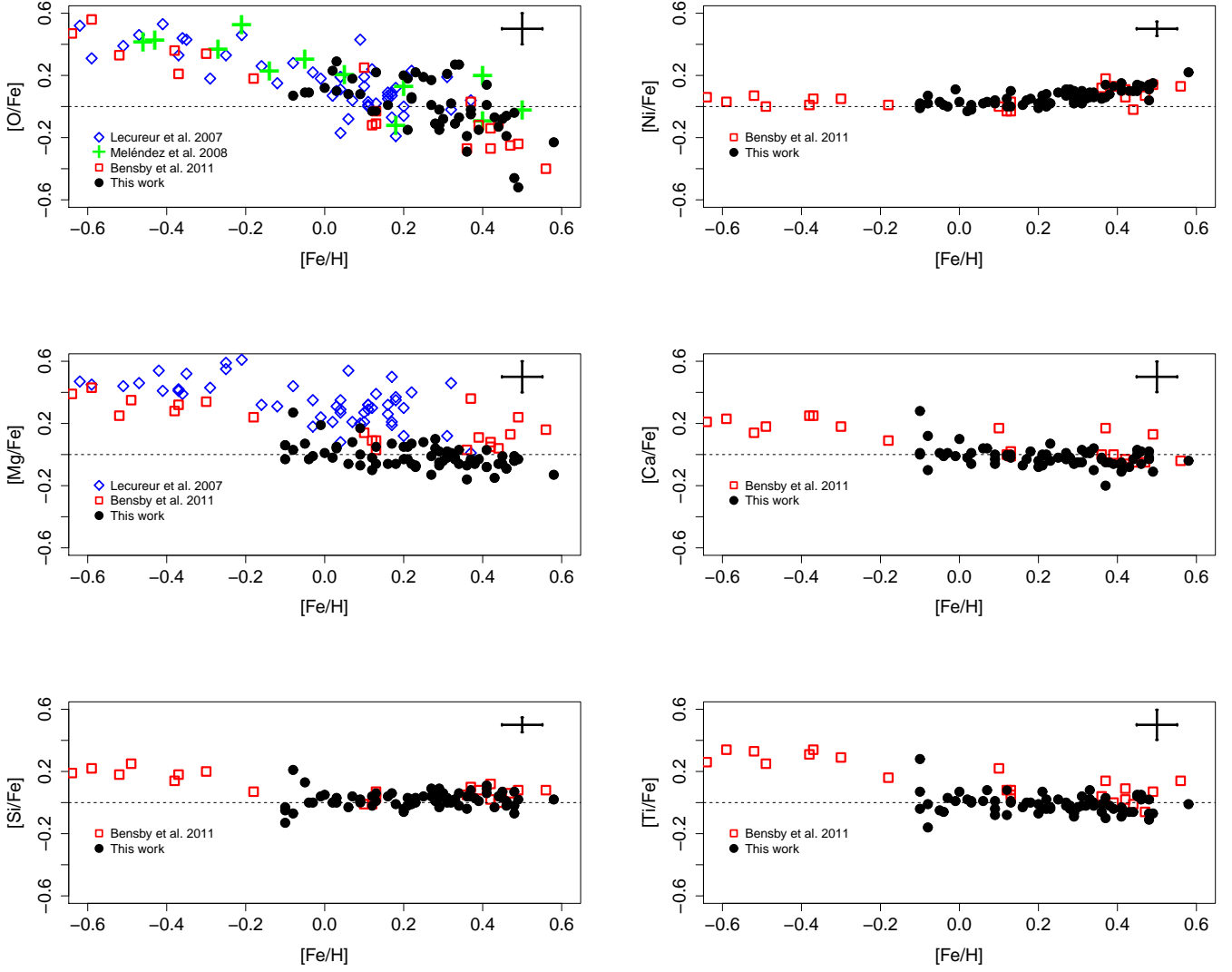


Fig. 26: Abundances of O, Ni, Mg, Ca, Si, and Ti vs.  $[\text{Fe}/\text{H}]$ . Sample stars from thick disk are indicated as black dots, blue diamonds, green crosses, and red squares are bulge stars from Lecureur et al. (2007), Meléndez et al. (2008), and bulge microlensed dwarfs by Bensby et al. (2011), respectively.

(2008) interprets these stars as old thin disk, or transition objects between the two disks, but as closer to an old thin disk. Our subsample has higher metallicities than Haywood’s subsample and could have an origin closer to the Galactic centre than Haywood’s old thin disk/transition component.

The presence of very metal-rich stars in the solar neighbourhood, at a relatively low rotational velocity give evidence of radial migration in the Galaxy, induced by the bar and/or interaction of bar and spiral arms, such as proposed by Fux (1997), Rouboud et al. (1998), Sellwood & Binney (2002), Lépine et al. (2003), Haywood (2008), Minchev & Famaey (2010), (Schönrich & Binney 2009a,b), or Brunetti et al. (2010).

Finally, we can conclude that the sample stars, all metal-rich, should be old thin stars from the inner disk, as suggested by Haywood (2008), including the 42 ones identified to have kinematics of the thick disk, and  $[\alpha/\text{Fe}] < +0.1$ . On the other hand, it is natural that the very metal-rich stars have low  $\alpha$ -to-iron ratios, as discussed in Roskar et al. (2011), i.e. all stars with  $[\text{Fe}/\text{H}] > 0$  show such low  $\alpha$ -to-iron. In other words, the decreasing trend of

$[\alpha\text{-elements}/\text{Fe}]$  with increasing metallicity means that the SNIa enrichment in iron occurs at the same pace for our sample, thick disk, and bulge stars. Therefore, for identifying bulge stars and thick disk as a same population, as suggested by Bensby et al. (2011), this cannot be inferred from the present results.

## Acknowledgments

The observations were carried out within Brazilian time in an ESO-ON agreement and within an IAG-ON agreement funded by FAPESP project n° 1998/10138-8. We thank the referee for the very insightful comments that led to a number of significant improvements in our manuscript. We are grateful to Giovanni Carraro for sharing his GRINTON integrator code used in Galactic orbits calculations. BB acknowledges partial financial support from CNPq and Fapesp. MT acknowledges an FAPESP fellowship no. 2008/50198-3.

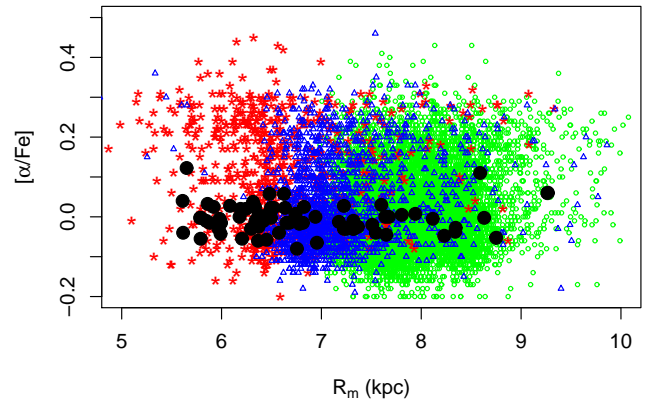
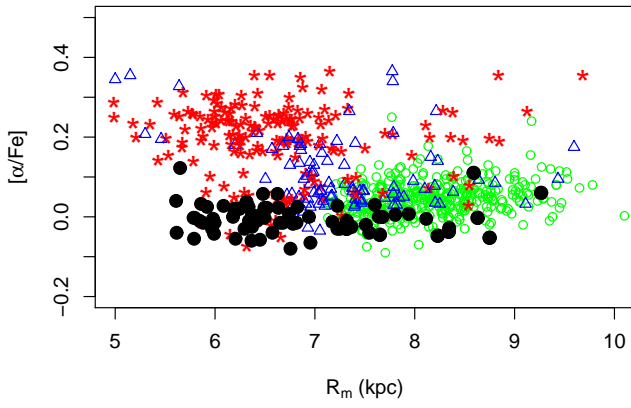
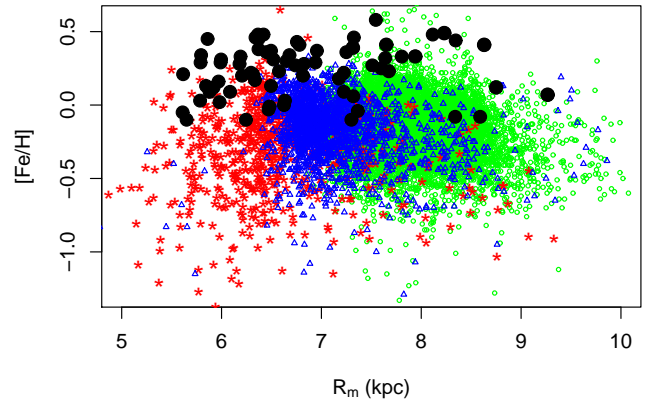
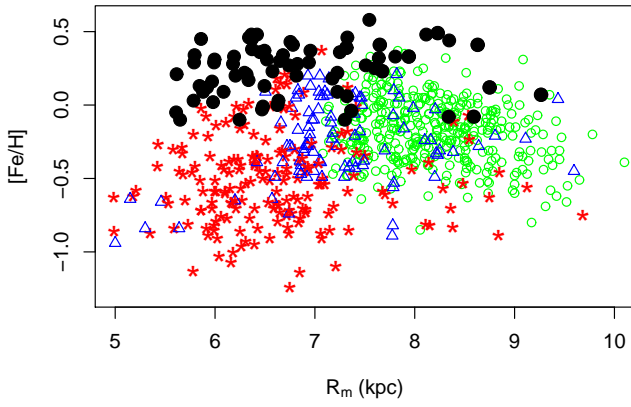


Fig. 27: Mean Galactocentric distance vs.  $[Fe/H]$  (*top*)  $[alpha/Fe]$  (*bottom*). Stars belonging to thin disk, thick disk, and intermediate populations are indicated as green circles, red stars, and blue triangles, respectively.

Fig. 28: Mean Galactocentric distance vs.  $[Fe/H]$  (*top*)  $[alpha/Fe]$  (*bottom*) for the GCS stars. Symbols are the same as Fig. 27.

## References

- Allen, C. & Santillan, A. 1991, *RMxAA*, 22, 255
- Allende Prieto, C., Barklem, P. S., Lambert, D. L., & Cunha, K. 2004, *A&A*, 420, 183
- Allende Prieto, C. & Lambert, D. L. 1999, *A&A*, 352, 555
- Alonso, A., Arribas, S., & Martínez-Roger, C. 1994, *A&AS*, 107, 365
- Alonso, A., Arribas, S., & Martínez-Roger, C. 1995, *A&A*, 297, 197
- Alonso, A., Arribas, S., & Martínez-Roger, C. 1996, *A&A*, 313, 873
- Alonso, A., Arribas, S., & Martínez-Roger, C. 1999, *A&AS*, 139, 335
- Asplund, M., Grevesse, N., & Sauval, A. J. 2005, in *Astronomical Society of the Pacific Conference Series*, Vol. 336, *Cosmic Abundances as Records of Stellar Evolution and Nucleosynthesis*, ed. T. G. Barnes III & F. N. Bash, 25
- Barbuy, B. 2007, *Transactions of the International Astronomical Union*, XXVB, 135
- Barbuy, B., Perrin, M.-N., Katz, D., et al. 2003, *A&A*, 404, 661
- Barbuy, B., Zoccali, M., Ortolani, S., et al. 2009, *A&A*, 507, 405
- Barklem, P. S., Anstee, S. D., & O'Mara, B. J. 1998, *Publications of the Astronomical Society of Australia*, 15, 336
- Barklem, P. S. & Asplund-Johansson, J. 2005, *A&A*, 435, 373
- Barklem, P. S., Piskunov, N., & O'Mara, B. J. 2000, *A&AS*, 142, 467
- Bedin, L. R., Piotto, G., Carraro, G., King, I. R., & Anderson, J. 2006, *A&A*, 460, L27
- Bensby, T., Adén, D., Meléndez, J., et al. 2011
- Bensby, T., Feltzing, S., & Lundström, I. 2003, *A&A*, 410, 527
- Bensby, T., Feltzing, S., & Lundström, I. 2004, *A&A*, 415, 155
- Bensby, T., Feltzing, S., Lundström, I., & Ilyin, I. 2005, *A&A*, 433, 185
- Brunetti, M., Chiappini, C., & Pfenninger, D. 2010, *ArXiv e-prints*
- Carpenter, J. M. 2001, *AJ*, 121, 2851
- Carraro, G., Girardi, L., & Marigo, P. 2002, *MNRAS*, 332, 705
- Casagrande, L., Portinari, L., & Flynn, C. 2006, *MNRAS*, 373, 13
- Casagrande, L., Ramírez, I., Meléndez, J., Bessell, M., & Asplund, M. 2010, *A&A*, 512, A54+
- Casagrande, L., Schoenrich, R., Asplund, M., et al. 2011, *ArXiv e-prints*
- Castro, S., Rich, R. M., Grenon, M., Barbuy, B., & McCarthy, J. K. 1997, *AJ*, 114, 376
- Cayrel, R., Perrin, M.-N., Barbuy, B., & Buser, R. 1991, *A&A*, 247, 108
- Chen, B., Vergely, J. L., Valette, B., & Carraro, G. 1998, *A&A*, 336, 137
- Chiba, M. & Beers, T. C. 2000, *AJ*, 119, 2843
- Coelho, P., Barbuy, B., Meléndez, J., Schiavon, R. P., & Castilho, B. V. 2005, *A&A*, 443, 735
- Cohen, J. G., Thompson, I. B., Sumi, T., et al. 2009, *ApJ*, 699, 66
- da Silva, L., Girardi, L., Pasquini, L., et al. 2006, *A&A*, 458, 609
- Dehnen, W. & Binney, J. J. 1998, *MNRAS*, 298, 387
- Demarque, P., Woo, J., Kim, Y., & Yi, S. K. 2004, *ApJS*, 155, 667
- Edvardsson, B., Andersen, J., Gustafsson, B., et al. 1993, *A&A*, 275, 101
- ESA. 1997, *VizieR Online Data Catalog*, 1239, 0
- Famaey, B., Jorissen, A., Luri, X., et al. 2005, *A&A*, 430, 165
- Feltzing, S., Bensby, T., & Lundström, I. 2003, *A&A*, 397, L1
- Feltzing, S. & Gustafsson, B. 1998, *A&AS*, 129, 237
- Fuhr, J. R. & Wiese, W. L. 2006, *Journal of Physical and Chemical Reference Data*, 35, 1669
- Fuhrmann, K. 1998, *A&A*, 338, 161
- Fux, R. 1997, *A&A*, 327, 983
- Geltman, S. 1962, *ApJ*, 136, 935
- Gingerich, O. 1964, 167, 17
- Girardi, L., Bressan, A., Bertelli, G., & Chiosi, C. 2000, *A&AS*, 141, 371
- Gonzalez, O. A., Rejkuba, M., Zoccali, M., et al. 2011, *A&A*, 530, A54
- González Hernández, J. I. & Bonifacio, P. 2009, *A&A*, 497, 497
- Gratton, R. G., Carretta, E., Matteucci, F., & Sneden, C. 2000, *A&A*, 358, 671
- Grenon, M. 1972, in *IAU Colloq. 17: Age des Etoiles*, ed. G. Cayrel de Strobel & A. M. Delplace, 55
- Grenon, M. 1978, *Photometric properties of G, K and M stars in relation to galactic structure and evolution*, ed. Grenon, M.
- Grenon, M. 1989, *Ap&SS*, 156, 29
- Grenon, M. 1990, in *European Southern Observatory Conference and Workshop Proceedings*, Vol. 35, *European Southern Observatory Conference and Workshop Proceedings*, ed. B. J. Jarvis & D. M. Terndrup, 143–150
- Grenon, M. 1998, *Highlights of Astronomy*, 11, 560
- Grenon, M. 1999, *Ap&SS*, 265, 331
- Grenon, M. 2000, in *The Evolution of the Milky Way: Stars versus Clusters*, ed. F. Matteucci & F. Giovannelli, 47
- Grevesse, N., Noels, A., & Sauval, A. J. 1996, in *Astronomical Society of the Pacific Conference Series*, Vol. 99, *Cosmic Abundances*, ed. S. S. Holt & G. Sonneborn, 117
- Grevesse, N. & Sauval, A. J. 1998, *SSRv*, 85, 161
- Gustafsson, B., Edvardsson, B., Eriksson, K., et al. 2008, *A&A*, 486, 951
- Haywood, M. 2008, *MNRAS*, 388, 1175
- Holmberg, J., Nordström, B., & Andersen, J. 2009, *A&A*, 501, 941
- Ivezić, Z., Sesar, B., Jurić, M., et al. 2008, *ApJ*, 684, 287
- John, T. L. 1988, *A&A*, 193, 189
- Jurić, M., Ž. Ivezić, Brooks, A., et al. 2008, *ApJ*, 673, 864
- Katz, D., Soubiran, C., Cayrel, R., et al. 2011, *A&A*, 525, A90+
- Kaufer, A., Stahl, O., Tubbesing, S., et al. 2000, in *Presented at the Society of Photo-Optical Instrumentation Engineers (SPIE) Conference*, Vol. 4008, *Society of Photo-Optical Instrumentation Engineers (SPIE) Conference Series*, ed. M. Iye & A. F. Moorwood, 459–466
- Kupka, F., Piskunov, N., Ryabchikova, T. A., Stempels, H. C., & Weiss, W. W. 1999, *A&AS*, 138, 119
- Lecureur, A., Hill, V., Zoccali, M., et al. 2007, *A&A*, 465, 799
- Lépine, J. R. D., Acharova, I. A., & Mishurov, Y. N. 2003, *ApJ*, 589, 210
- Masana, E., Jordi, C., & Ribas, I. 2006, *A&A*, 450, 735
- McWilliam, A. 1990, *ApJS*, 74, 1075
- Meléndez, J., Asplund, M., Alves-Brito, A., et al. 2008, *A&A*, 484, L21
- Meléndez, J., Asplund, M., Gustafsson, B., & Yong, D. 2009, *ApJ*, 704, L66
- Meléndez, J. & Barbuy, B. 2009, *A&A*, 497, 611
- Meléndez, J. & Cohen, J. G. 2009, *ApJ*, 699, 2017
- Meléndez, J. & Ramírez, I. 2005, in *Astronomical Society of the Pacific Conference Series*, Vol. 336, *Cosmic Abundances as Records of Stellar Evolution and Nucleosynthesis*, ed. T. G. Barnes III & F. N. Bash, 343–+
- Minchev, I. & Famaey, B. 2010, *ApJ*, 722, 112
- Mishenina, T. V., Soubiran, C., Bienaymé, O., et al. 2008, *A&A*, 489, 923
- Mishenina, T. V., Soubiran, C., Kovtyukh, V. V., & Korotín, S. A. 2004, *A&A*, 418, 551
- Neves, V., Santos, N. C., Sousa, S. G., Correia, A. C. M., & Israelian, G. 2009, *A&A*, 497, 563
- Pompéia, L., Barbuy, B., & Grenon, M. 2002, *ApJ*, 566, 845
- Pompéia, L., Barbuy, B., & Grenon, M. 2003, *ApJ*, 592, 1173
- Pompéia, L., Barbuy, B., Grenon, M., & Gustafsson, B. 2007, in *IAU Symposium*, Vol. 241, *IAU Symposium*, ed. A. Vazdekis & R. F. Peletier, 78–81
- Raboud, D., Grenon, M., Martinet, L., Fux, R., & Udry, S. 1998, *A&A*, 335, L61
- Ramírez, I. & Meléndez, J. 2005, *ApJ*, 626, 446
- Reddy, B. E. & Lambert, D. L. 2008, *MNRAS*, 391, 95
- Reddy, B. E., Lambert, D. L., & Allende Prieto, C. 2006, *MNRAS*, 367, 1329
- Reddy, B. E., Tomkin, J., Lambert, D. L., & Allende Prieto, C. 2003, *MNRAS*, 340, 304
- Robin, A. C., Reylé, C., Derrière, S., & Picaud, S. 2003, *A&A*, 409, 523
- Roškar, R., Debattista, V. P., Loebman, S. R., Ž. Ivezić, & Quinn, T. R. 2011, *ArXiv e-prints*
- Ruchti, G. R., Fulbright, J. P., Wyse, R. F. G., et al. 2010, 721, L92
- Schönrich, R. & Binney, J. 2009a, *MNRAS*, 396, 203
- Schönrich, R. & Binney, J. 2009b, *MNRAS*, 399, 1145
- Schuster, W. J. & Nissen, P. E. 1989, *A&A*, 221, 65
- Sellwood, J. A. & Binney, J. J. 2002, *MNRAS*, 336, 785
- Skrutskie, M. F., Cutri, R. M., Stiening, R., et al. 2006, *AJ*, 131, 1163
- Soubiran, C., Bienaymé, O., & Siebert, A. 2003, *A&A*, 398, 141
- Soubiran, C. & Girard, P. 2005, *A&A*, 438, 139
- Soubiran, C., Le Campion, J., Cayrel de Strobel, G., & Caillo, A. 2010, *A&A*, 515, A111+
- Sousa, S. G., Santos, N. C., Israelian, G., Mayor, M., & Monteiro, M. J. P. F. G. 2006, *A&A*, 458, 873
- Sousa, S. G., Santos, N. C., Israelian, G., Mayor, M., & Monteiro, M. J. P. F. G. 2007, *A&A*, 469, 783
- Sousa, S. G., Santos, N. C., Mayor, M., et al. 2008, *A&A*, 487, 373
- Spite, M. 1967, *Annales d'Astrophysique*, 30, 211
- Spite, M., Huille, S., Spite, F., & Francois, P. 1987, *A&AS*, 71, 591
- Spite, M., Spite, F., & Barbuy, B. 1989, *A&A*, 222, 35
- Thévenin, F. & Idiart, T. P. 1999, *ApJ*, 521, 753
- Torres, G., Andersen, J., & Giménez, A. 2010, *A&ARv*, 18, 67
- Valenti, J. A. & Fischer, D. A. 2005, *ApJS*, 159, 141
- Villalobos, Á., Kazantzidis, S., & Helmi, A. 2010, *ApJ*, 718, 314
- Wallace, L., Hinkle, K., & Livingston, W. 1998, *An atlas of the spectrum of the solar photosphere from 13,500 to 28,000 cm<sup>-1</sup> (3570 to 7405 Å)*, ed. L. Wallace, K. Hinkle, & W. Livingston
- Wishart, A. W. 1979, *MNRAS*, 187, 59P
- Zoccali, M., Hill, V., Lecureur, A., et al. 2008, *A&A*, 486, 177





Table 13: Photometric and adopted spectroscopic stellar parameters

Star	$T_{\text{eff}}$ K	$\log g$ dex	$\xi$ km s <sup>-1</sup>	[Fe I/H] <sub>Gen</sub> dex	[Fe I/H] dex	[Fe II/H] dex	Mass ( $M_{\odot}$ )	Age (Gyr)
(1)	(2)	(3)	(4)	(5)	(6)	(7)		
Thin disk								
HD 11608	4966 ± 47	4.57 ± 0.06	0.30 ± 0.31	0.60	0.39 ± 0.05	0.42 ± 0.13	0.88 ± 0.06	5.6 ± 2.9
HD 26151	5383 ± 47	4.41 ± 0.05	0.67 ± 0.03	0.42	0.33 ± 0.05	0.34 ± 0.08	0.97 ± 0.07	8.2 ± 2.4
HD 26794	4920 ± 52	4.49 ± 0.06	0.30 ± 0.12	0.30	0.07 ± 0.04	0.10 ± 0.12	0.78 ± 0.05	11.8 ± 2.2
HD 35854	4901 ± 37	4.57 ± 0.03	0.30 ± 0.09	0.33	-0.04 ± 0.03	-0.00 ± 0.12	0.76 ± 0.05	9.0 ± 0.8
HD 77338	5346 ± 42	4.55 ± 0.05	0.44 ± 0.08	0.43	0.41 ± 0.05	0.49 ± 0.08	0.98 ± 0.07	2.0 ± 1.2
HD 82943	5929 ± 45	4.35 ± 0.04	1.22 ± 0.03	0.34	0.23 ± 0.05	0.26 ± 0.07	1.14 ± 0.08	3.0 ± 0.7
HD 86249	4957 ± 42	4.59 ± 0.05	0.30 ± 0.11	0.32	0.12 ± 0.04	0.20 ± 0.10	0.82 ± 0.06	7.3 ± 2.1
HD 93800	5181 ± 43	4.44 ± 0.07	0.30 ± 0.09	0.43	0.49 ± 0.04	0.57 ± 0.09	0.92 ± 0.07	8.8 ± 3.5
HD 177374	5044 ± 45	4.38 ± 0.08	0.30 ± 0.10	0.40	-0.08 ± 0.04	0.12 ± 0.10	0.79 ± 0.05	13.7 ± 1.0
HD 181433	4902 ± 41	4.57 ± 0.04	0.30 ± 0.21	0.65	0.41 ± 0.04	0.52 ± 0.12	0.86 ± 0.06	6.7 ± 1.8
HD 224230	4873 ± 54	4.58 ± 0.06	0.30 ± 0.17	0.34	-0.08 ± 0.04	0.11 ± 0.13	0.75 ± 0.05	9.4 ± 2.4
Thick disk								
G 161-029	4798 ± 34	4.60 <sup>a</sup> ± 0.04	0.30 ± 0.63	0.42	0.01 ± 0.09	0.12 ± 0.13	...	...
BD-02 180	5004 ± 57	4.46 ± 0.10	0.30 ± 0.17	0.45	0.33 ± 0.04	0.45 ± 0.08	0.86 ± 0.06	10.3 ± 4.0
BD-05 5798	4902 ± 65	4.44 ± 0.13	0.64 ± 0.05	0.57	0.20 ± 0.05	0.27 ± 0.13	0.82 ± 0.06	11.4 ± 3.7
BD-17 6035	4892 ± 73	4.43 ± 0.15	0.85 ± 0.03	0.60	0.09 ± 0.05	0.17 ± 0.14	0.79 ± 0.06	11.5 ± 3.2
CD-32 0327	4957 ± 66	4.52 ± 0.11	0.34 ± 0.06	0.49	-0.01 ± 0.06	0.19 ± 0.10	0.79 ± 0.05	10.3 ± 3.5
CD-40 15036	5429 ± 66	4.41 ± 0.14	0.58 ± 0.04	0.07	-0.03 ± 0.07	-0.03 ± 0.09	0.89 ± 0.07	9.8 ± 4.6
HD 9424	5449 ± 48	4.48 ± 0.06	0.66 ± 0.03	0.12	0.12 ± 0.06	0.10 ± 0.08	0.95 ± 0.07	6.1 ± 3.2
HD 10576	5929 ± 67	4.14 ± 0.06	1.36 ± 0.06	0.11	0.02 ± 0.07	0.02 ± 0.08	1.12 ± 0.08	5.8 ± 0.9
HD 13386	5269 ± 43	4.54 ± 0.05	0.46 ± 0.04	0.35	0.36 ± 0.05	0.34 ± 0.09	0.96 ± 0.07	3.6 ± 2.4
HD 15133	5223 ± 46	4.47 ± 0.08	0.30 ± 0.05	0.52	0.46 ± 0.04	0.51 ± 0.09	0.94 ± 0.07	6.9 ± 3.7
HD 15555	4867 ± 40	3.69 ± 0.06	1.04 ± 0.03	0.32	0.37 ± 0.05	0.38 ± 0.11	1.22 ± 0.10	6.3 ± 0.9
HD 16905	4866 ± 42	4.58 ± 0.05	0.30 ± 0.14	0.53	0.27 ± 0.04	0.44 ± 0.12	0.83 ± 0.06	7.4 ± 1.8
HD 25061	5307 ± 49	4.49 ± 0.05	0.77 ± 0.03	0.40	0.18 ± 0.05	0.19 ± 0.09	0.92 ± 0.06	6.7 ± 3.3
HD 27894	4920 ± 45	4.54 ± 0.05	0.30 ± 0.12	0.50	0.37 ± 0.04	0.51 ± 0.10	0.86 ± 0.06	7.7 ± 2.3
HD 31827	5608 ± 49	4.35 ± 0.04	0.82 ± 0.03	0.40	0.48 ± 0.05	0.49 ± 0.08	1.08 ± 0.07	4.8 ± 0.9
HD 39213	5473 ± 48	4.38 ± 0.06	0.74 ± 0.04	0.39	0.45 ± 0.06	0.44 ± 0.08	1.02 ± 0.07	6.3 ± 2.0
HD 81767	4966 ± 52	4.49 ± 0.07	0.30 ± 0.11	0.49	0.22 ± 0.05	0.25 ± 0.13	0.83 ± 0.05	10.4 ± 3.0
HD 90054	6047 ± 52	4.18 ± 0.06	1.52 ± 0.05	0.39	0.29 ± 0.06	0.33 ± 0.07	1.28 ± 0.08	3.2 ± 0.4
HD 94374	5000 ± 38	4.63 ± 0.05	0.30 ± 0.08	0.28	-0.10 ± 0.03	-0.18 ± 0.13	0.79 ± 0.05	4.8 ± 2.4
HD 95338	5175 ± 42	4.52 ± 0.04	0.43 ± 0.05	0.34	0.21 ± 0.04	0.22 ± 0.09	0.90 ± 0.06	6.3 ± 2.6
HD 104212	5833 ± 53	4.07 ± 0.09	1.21 ± 0.03	0.09	0.13 ± 0.06	0.07 ± 0.07	1.14 ± 0.08	5.9 ± 0.8
HD 107509	6102 ± 60	4.18 ± 0.06	1.80 ± 0.06	0.08	0.03 ± 0.06	-0.06 ± 0.08	1.21 ± 0.09	3.9 ± 0.5
HD 120329	5617 ± 48	4.14 ± 0.07	1.22 ± 0.02	0.27	0.31 ± 0.06	0.39 ± 0.07	1.11 ± 0.08	7.3 ± 1.0
HD 143102	5547 ± 48	3.94 ± 0.07	1.13 ± 0.03	0.01	0.16 ± 0.06	0.21 ± 0.08	1.16 ± 0.08	6.8 ± 1.0
HD 148530	5392 ± 53	4.49 ± 0.06	0.72 ± 0.04	0.11	0.03 ± 0.06	0.02 ± 0.09	0.90 ± 0.08	7.1 ± 3.6
HD 149256	5406 ± 47	4.01 ± 0.08	1.15 ± 0.02	0.27	0.34 ± 0.06	0.38 ± 0.08	1.08 ± 0.08	8.9 ± 1.5
HD 149606	4976 ± 50	4.63 ± 0.05	0.30 ± 0.08	0.35	0.20 ± 0.05	0.41 ± 0.11	0.85 ± 0.10	4.1 ± 2.6
HD 149933	5486 ± 49	4.44 ± 0.05	1.11 ± 0.02	0.31	0.13 ± 0.06	0.17 ± 0.08	0.95 ± 0.06	7.2 ± 2.9
HD 165920	5336 ± 44	4.47 ± 0.04	0.64 ± 0.03	0.40	0.36 ± 0.05	0.40 ± 0.08	0.97 ± 0.07	5.2 ± 2.5
HD 168714	5686 ± 48	4.30 ± 0.11	0.79 ± 0.03	0.47	0.48 ± 0.06	0.47 ± 0.08	1.12 ± 0.07	4.0 ± 1.1
HD 171999	5304 ± 45	4.49 ± 0.05	0.58 ± 0.03	0.33	0.29 ± 0.05	0.35 ± 0.08	0.96 ± 0.09	6.0 ± 2.8
HD 179764	5323 ± 48	4.28 ± 0.08	0.92 ± 0.04	0.16	-0.05 ± 0.05	0.03 ± 0.09	0.85 ± 0.06	14.6 ± 0.6
HD 180865	5218 ± 44	4.53 ± 0.06	0.48 ± 0.06	0.31	0.21 ± 0.05	0.27 ± 0.09	0.91 ± 0.06	5.9 ± 3.1
HD 181234	5311 ± 45	4.37 ± 0.06	0.30 ± 0.07	0.30	0.45 ± 0.04	0.52 ± 0.09	0.96 ± 0.06	9.4 ± 2.2
HD 196397	5404 ± 54	4.49 ± 0.08	0.55 ± 0.07	0.36	0.38 ± 0.06	0.43 ± 0.09	0.99 ± 0.07	3.7 ± 2.8
HD 201237	4829 ± 82	4.14 ± 0.16	0.50 ± 0.05	0.50	0.00 ± 0.04	-0.06 ± 0.18	0.77 ± 0.05	13.8 ± 0.9
HD 209721	5503 ± 51	4.30 ± 0.10	1.05 ± 0.03	0.35	0.28 ± 0.05	0.23 ± 0.08	1.00 ± 0.08	8.8 ± 2.1
HD 211706	6017 ± 69	4.33 ± 0.11	1.44 ± 0.08	0.09	0.09 ± 0.07	0.07 ± 0.08	1.14 ± 0.08	3.0 ± 1.5
HD 218566	4849 ± 42	4.48 ± 0.04	0.30 ± 0.68	0.49	0.28 ± 0.14	0.43 ± 0.22	0.81 ± 0.06	11.5 ± 1.9
HD 218750	5134 ± 49	4.41 ± 0.08	0.37 ± 0.08	0.31	0.17 ± 0.05	0.23 ± 0.09	0.85 ± 0.06	12.8 ± 2.4
HD 221313	5153 ± 55	4.36 ± 0.13	0.62 ± 0.04	0.50	0.31 ± 0.05	0.34 ± 0.10	0.90 ± 0.06	12.0 ± 3.6
HD 221974	5213 ± 52	4.60 ± 0.07	0.30 ± 0.11	0.49	0.46 ± 0.05	0.56 ± 0.11	0.95 ± 0.07	2.2 ± 1.8
HD 224383	5760 ± 53	4.28 ± 0.06	1.16 ± 0.09	0.00	-0.10 ± 0.06	-0.15 ± 0.08	0.98 ± 0.07	9.0 ± 1.3
Intermediate population								
HD 8389	5274 ± 42	4.47 ± 0.04	0.33 ± 0.12	0.47	0.58 ± 0.04	0.58 ± 0.08	0.96 ± 0.07	5.4 ± 1.8
HD 9174	5599 ± 55	4.15 ± 0.08	0.95 ± 0.02	0.36	0.41 ± 0.07	0.35 ± 0.08	1.13 ± 0.08	6.7 ± 1.0
HD 12789	5810 ± 47	4.21 ± 0.09	1.15 ± 0.03	0.31	0.27 ± 0.06	0.36 ± 0.07	1.17 ± 0.08	4.9 ± 0.9
HD 30295	5406 ± 45	4.36 ± 0.05	0.72 ± 0.03	0.41	0.32 ± 0.05	0.33 ± 0.08	0.97 ± 0.07	9.1 ± 1.8
HD 31452	5250 ± 45	4.44 ± 0.05	0.61 ± 0.05	0.30	0.23 ± 0.05	0.19 ± 0.09	0.90 ± 0.06	10.0 ± 3.1
HD 37986	5503 ± 44	4.47 ± 0.04	0.95 ± 0.02	0.47	0.30 ± 0.05	0.33 ± 0.08	1.02 ± 0.07	4.0 ± 1.6
HD 39715	4741 ± 63	4.57 ± 0.04	0.30 ± 0.15	0.33	-0.10 ± 0.03	0.07 ± 0.15	0.72 ± 0.05	9.6 ± 1.6
HD 43848	5161 ± 41	4.54 ± 0.04	0.30 ± 0.08	0.52	0.43 ± 0.04	0.46 ± 0.09	0.94 ± 0.06	3.7 ± 1.7
HD 86065	4938 ± 48	4.62 ± 0.05	0.30 ± 0.10	0.36	0.09 ± 0.04	0.21 ± 0.12	0.82 ± 0.06	6.0 ± 2.6
HD 87007	5282 ± 59	4.54 ± 0.06	0.61 ± 0.04	0.44	0.29 ± 0.06	0.45 ± 0.09	0.95 ± 0.06	4.0 ± 2.9
HD 91585	5144 ± 50	4.55 ± 0.07	0.48 ± 0.07	0.30	0.25 ± 0.05	0.33 ± 0.10	0.91 ± 0.09	5.4 ± 3.5
HD 91669	5278 ± 57	4.34 ± 0.11	0.64 ± 0.04	0.42	0.44 ± 0.05	0.45 ± 0.09	0.95 ± 0.06	10.1 ± 3.4
HD 182572	5700 ± 32	4.18 ± 0.03	1.00 ± 0.02	0.31	0.48 ± 0.04	0.39 ± 0.07	1.16 ± 0.07	4.5 ± 0.2
HD 196794	5094 ± 44	4.64 ± 0.04	0.30 ± 0.05	0.33	0.06 ± 0.05	0.16 ± 0.09	0.84 ± 0.06	3.7 ± 2.0
HD 197921	4866 ± 45	4.48 ± 0.06	0.30 ± 0.15	0.39	0.22 ± 0.04	0.33 ± 0.10	0.80 ± 0.05	11.3 ± 2.4
HD 213996	5314 ± 53	4.49 ± 0.05	0.75 ± 0.04	0.43	0.33 ± 0.05	0.35 ± 0.10	0.96 ± 0.09	5.1 ± 3.0
HD 214463	5122 ± 47	4.40 ± 0.11	0.80 ± 0.04	0.33	0.34 ± 0.05	0.30 ± 0.09	0.90 ± 0.06	11.8 ± 3.7

Notes. <sup>(a)</sup> Spectroscopic gravity. Other  $\log g$ s were derived using HIPPARCOS parallaxes.

Table 14: Final abundances

Star	[C/H]	[C/Fe]	[Ni/H]	[Ni/Fe]	[O/H]	[O/Fe]	[Mg/H]	[Mg/Fe]
Thin disk								
HD 11608	0.26	-0.13	0.52 ± 0.06	0.13	0.24	-0.15	0.36	-0.03
HD 26151	0.24	-0.09	0.42 ± 0.05	0.09	...	...	0.31	-0.02
HD 26794	0.07	-0.00	0.10 ± 0.03	0.03	0.25	0.18	0.15	0.08
HD 35854	-0.00	0.04	-0.03 ± 0.03	0.01	0.05	0.09	-0.07	-0.03
HD 77338	0.44	0.03	0.52 ± 0.04	0.11	...	...	0.33	-0.08
HD 82943	0.18	-0.05	0.25 ± 0.06	0.02	0.45	0.22	0.16	-0.07
HD 86249	0.15	0.03	0.12 ± 0.03	0.00	...	...	0.02	-0.10
HD 93800	0.44	-0.05	0.64 ± 0.04	0.15	-0.03	-0.52	0.46	-0.03
HD 177374	0.32	0.40	-0.01 ± 0.03	0.07	...	...	0.19	0.27
HD 181433	...	...	0.56 ± 0.04	0.15	0.42	0.01	0.44	0.03
HD 224230	0.10	0.18	-0.05 ± 0.03	0.02	-0.01	0.07	-0.06	0.03
Thick disk								
G 161-029	0.04	0.03	0.10 ± 0.09	0.08	...	...	0.10	0.09
BD-02 180	0.35	0.02	0.41 ± 0.04	0.08	0.60	0.27	0.30	-0.03
BD-05 5798	0.28	0.08	0.19 ± 0.04	-0.01	...	...	0.25	0.05
BD-17 6035	0.31	0.22	0.12 ± 0.04	0.03	...	...	0.26	0.17
CD-32 0327	...	...	0.09 ± 0.04	0.11	...	...	0.11	0.19
CD-40 15036	-0.01	0.02	-0.02 ± 0.07	0.00	...	...	-0.14	-0.01
HD 9424	0.17	0.05	0.17 ± 0.05	0.05	0.09	-0.03	0.10	-0.02
HD 10576	...	...	-0.01 ± 0.07	-0.03	0.25	0.23	0.00	-0.02
HD 13386	0.25	-0.11	0.41 ± 0.04	0.05	0.07	-0.29	0.30	-0.16
HD 15133	0.25	-0.21	0.59 ± 0.04	0.13	0.27	-0.19	0.37	-0.09
HD 15555	-0.11	-0.48	0.51 ± 0.04	0.14	0.35	-0.02	0.33	-0.04
HD 16905	0.23	-0.04	0.38 ± 0.04	0.11	0.28	0.01	0.26	-0.01
HD 25061	0.13	-0.05	0.23 ± 0.04	0.05	...	...	0.12	-0.06
HD 27894	0.25	-0.12	0.43 ± 0.04	0.06	0.32	-0.05	0.34	-0.03
HD 31827	0.46	-0.02	0.59 ± 0.05	0.11	0.02	-0.46	0.47	-0.01
HD 39213	...	...	0.59 ± 0.05	0.14	...	...	0.39	-0.06
HD 81767	-0.01	-0.23	0.22 ± 0.03	0.00	0.28	0.06	0.16	-0.06
HD 90054	0.31	0.02	0.31 ± 0.06	0.02	0.17	-0.12	0.22	-0.07
HD 94374	0.25	0.35	-0.08 ± 0.03	0.02	...	...	-0.04	0.06
HD 95338	0.06	-0.15	0.25 ± 0.04	0.04	0.06	-0.15	0.18	-0.03
HD 104212	0.11	-0.02	0.13 ± 0.07	0.00	0.35	0.22	0.07	-0.06
HD 107509	-0.05	-0.08	0.00 ± 0.07	-0.02	0.13	0.10	0.01	0.05
HD 120329	0.39	0.08	0.33 ± 0.06	0.02	...	...	0.29	-0.02
HD 143102	...	...	0.17 ± 0.06	0.01	0.17	0.01	0.10	-0.06
HD 148530	0.06	0.03	0.04 ± 0.05	0.01	0.32	0.29	0.07	0.04
HD 149256	...	...	0.40 ± 0.05	0.06	0.61	0.27	0.37	0.03
HD 149606	0.24	0.04	0.22 ± 0.04	0.02	0.40	0.20	0.17	-0.03
HD 149933	0.21	0.08	0.23 ± 0.05	0.10	0.10	-0.03	0.21	0.05
HD 165920	0.34	-0.02	0.42 ± 0.04	0.06	0.17	-0.19	0.29	-0.07
HD 168714	0.35	-0.13	0.62 ± 0.05	0.14	...	...	0.44	-0.04
HD 171999	0.30	0.01	0.33 ± 0.04	0.04	0.27	-0.02	0.24	-0.05
HD 179764	...	...	-0.02 ± 0.05	0.03	0.04	0.09	0.02	0.07
HD 180865	0.20	-0.01	0.28 ± 0.04	0.07	0.39	0.18	0.26	0.05
HD 181234	0.30	-0.15	0.55 ± 0.04	0.10	0.37	-0.08	0.44	-0.01
HD 196397	0.37	-0.01	0.46 ± 0.05	0.08	...	...	0.32	-0.06
HD 201237	-0.19	-0.19	0.03 ± 0.04	0.03	0.12	0.12	0.01	0.01
HD 209721	0.35	0.07	0.36 ± 0.05	0.08	0.17	-0.11	0.32	0.04
HD 211706	0.09	0.00	0.11 ± 0.08	0.02	...	...	0.02	-0.07
HD 218566	0.21	-0.07	0.39 ± 0.15	0.11	0.17	-0.11	0.12	0.10
HD 218750	0.22	0.05	0.21 ± 0.04	0.04	...	...	0.24	0.07
HD 221313	...	...	0.41 ± 0.04	0.10	0.52	0.21	0.33	0.02
HD 221974	0.39	-0.07	0.59 ± 0.04	0.13	0.40	-0.06	0.37	-0.09
HD 224383	-0.03	0.07	-0.10 ± 0.06	-0.01	...	...	-0.04	0.06
Intermediate population								
HD 8389	0.46	-0.12	0.71 ± 0.04	0.22	0.35	-0.23	0.45	-0.13
HD 9174	...	...	0.51 ± 0.06	0.10	0.55	0.14	0.33	-0.08
HD 12789	...	...	0.34 ± 0.06	0.07	0.44	0.17	0.14	-0.13
HD 30295	0.33	0.01	0.37 ± 0.04	0.05	0.34	0.02	0.33	0.01
HD 31452	...	...	0.25 ± 0.04	0.02	...	...	0.15	-0.08
HD 37986	0.34	0.04	0.35 ± 0.04	0.05	0.22	-0.08	0.26	-0.04
HD 39715	...	...	-0.10 ± 0.03	0.01	...	...	-0.13	-0.03
HD 43848	0.29	-0.14	0.53 ± 0.04	0.10	0.36	-0.07	0.38	-0.15
HD 86065	0.11	0.02	0.13 ± 0.04	0.04	0.17	0.08	0.09	-0.00
HD 87007	0.23	-0.06	0.39 ± 0.04	0.10	0.14	-0.15	0.31	0.02
HD 91585	0.28	0.03	0.34 ± 0.04	0.09	0.44	0.19	0.33	0.08
HD 91669	0.32	-0.12	0.54 ± 0.04	0.10	0.31	-0.13	0.38	-0.06
HD 182572	0.29	-0.19	0.52 ± 0.04	0.04	0.44	-0.04	0.44	-0.04
HD 196794	-0.02	-0.08	0.08 ± 0.04	0.02	0.14	0.08	0.00	-0.06
HD 197921	0.12	-0.10	0.30 ± 0.04	0.08	0.27	0.05	0.29	0.07
HD 213996	0.27	-0.06	0.39 ± 0.04	0.06	0.22	-0.11	0.30	-0.03
HD 214463	0.22	-0.12	0.43 ± 0.03	0.09	0.27	-0.07	0.28	-0.06

Table 15: Final abundances

Star	[Ca/H]	[Ca/Fe]	[Si/H]	[Si/Fe]	[Ti/H]	[Ti/Fe]
Thin disk						
HD 11608	0.33 ± 0.10	-0.06	0.40 ± 0.06	0.01	0.35 ± 0.09	-0.04
HD 26151	0.34 ± 0.04	0.01	0.35 ± 0.04	0.02	0.35 ± 0.09	0.02
HD 26794	0.11 ± 0.09	0.04	0.11 ± 0.05	0.04	0.15 ± 0.11	0.08
HD 35854	-0.05 ± 0.11	-0.01	-0.04 ± 0.05	-0.00	-0.10 ± 0.08	-0.06
HD 77338	0.34 ± 0.06	-0.07	0.47 ± 0.05	0.06	0.32 ± 0.08	-0.09
HD 82943	0.30 ± 0.05	0.07	0.26 ± 0.05	0.03	0.20 ± 0.07	-0.03
HD 86249	0.11 ± 0.10	-0.01	0.10 ± 0.05	-0.02	0.04 ± 0.09	-0.08
HD 93800	0.38 ± 0.10	-0.11	0.51 ± 0.05	0.02	0.42 ± 0.08	-0.07
HD 177374	0.04 ± 0.14	0.12	0.13 ± 0.05	0.21	-0.24 ± 0.09	-0.16
HD 181433	0.30 ± 0.13	-0.11	0.52 ± 0.05	0.11	0.37 ± 0.08	-0.04
HD 224230	-0.18 ± 0.20	-0.10	-0.14 ± 0.06	-0.07	-0.09 ± 0.11	-0.01
Thick disk						
G 161-029	0.00 ± 0.12	-0.01	0.05 ± 0.06	0.04	0.04 ± 0.12	0.02
BD-02 180	0.35 ± 0.04	0.02	0.34 ± 0.06	0.01	0.41 ± 0.11	0.08
BD-05 5798	0.16 ± 0.15	-0.04	0.14 ± 0.06	-0.06	0.19 ± 0.13	-0.01
BD-17 6035	0.06 ± 0.18	-0.03	0.10 ± 0.06	0.01	0.05 ± 0.17	-0.04
CD-32 0327	-0.02 ± 0.19	-0.01	0.03 ± 0.05	0.04	-0.01 ± 0.15	0.01
CD-40 15036	-0.02 ± 0.11	0.01	-0.03 ± 0.03	0.00	0.00 ± 0.12	0.03
HD 9424	0.12 ± 0.10	-0.00	0.16 ± 0.04	0.04	0.20 ± 0.09	0.08
HD 10576	-0.00 ± 0.11	-0.02	0.03 ± 0.05	0.00	0.04 ± 0.10	0.02
HD 13386	0.34 ± 0.08	-0.02	0.32 ± 0.05	-0.04	0.35 ± 0.09	-0.01
HD 15133	0.48 ± 0.10	0.02	0.44 ± 0.05	-0.02	0.51 ± 0.09	0.05
HD 15555	0.17 ± 0.08	-0.20	0.45 ± 0.05	0.08	0.27 ± 0.09	-0.10
HD 16905	0.24 ± 0.08	-0.03	0.36 ± 0.05	0.09	0.25 ± 0.09	-0.02
HD 25061	0.20 ± 0.09	0.02	0.17 ± 0.04	-0.01	0.18 ± 0.09	-0.00
HD 27894	0.32 ± 0.10	-0.05	0.41 ± 0.05	0.04	0.40 ± 0.10	0.03
HD 31827	0.45 ± 0.05	-0.03	0.55 ± 0.04	0.07	0.41 ± 0.09	-0.07
HD 39213	0.45 ± 0.05	-0.00	0.48 ± 0.04	0.03	0.50 ± 0.08	0.05
HD 81767	0.21 ± 0.09	-0.01	0.21 ± 0.05	-0.01	0.18 ± 0.11	-0.04
HD 90054	0.24 ± 0.15	-0.05	0.26 ± 0.05	-0.03	0.22 ± 0.08	-0.07
HD 94374	0.18 ± 0.09	0.28	-0.23 ± 0.04	-0.13	0.18 ± 0.08	0.28
HD 95338	0.14 ± 0.05	-0.07	0.19 ± 0.04	-0.02	0.17 ± 0.09	-0.04
HD 104212	0.13 ± 0.07	0.00	0.14 ± 0.04	0.01	0.14 ± 0.08	0.01
HD 107509	-0.03 ± 0.23	-0.06	0.03 ± 0.05	-0.00	0.02 ± 0.08	-0.00
HD 120329	0.26 ± 0.06	-0.05	0.34 ± 0.04	0.03	0.29 ± 0.09	-0.02
HD 143102	0.09 ± 0.06	-0.07	0.20 ± 0.04	0.04	0.13 ± 0.08	-0.03
HD 148530	0.04 ± 0.11	0.01	0.06 ± 0.04	0.03	0.04 ± 0.10	0.01
HD 149256	0.24 ± 0.08	-0.10	0.40 ± 0.05	0.06	0.34 ± 0.09	0.00
HD 149606	0.12 ± 0.14	-0.08	0.16 ± 0.05	-0.04	0.13 ± 0.10	-0.07
HD 149933	0.11 ± 0.12	-0.02	0.19 ± 0.04	0.06	0.13 ± 0.09	-0.00
HD 165920	0.33 ± 0.06	-0.03	0.40 ± 0.04	0.04	0.30 ± 0.08	-0.06
HD 168714	0.46 ± 0.12	-0.02	0.41 ± 0.04	-0.07	0.37 ± 0.09	-0.11
HD 171999	0.23 ± 0.10	-0.06	0.32 ± 0.04	0.03	0.20 ± 0.09	-0.09
HD 179764	-0.04 ± 0.06	0.01	0.08 ± 0.04	0.13	-0.10 ± 0.09	-0.05
HD 180865	0.21 ± 0.07	-0.00	0.24 ± 0.04	0.03	0.28 ± 0.10	0.07
HD 181234	0.48 ± 0.10	0.03	0.52 ± 0.04	0.07	0.49 ± 0.08	0.04
HD 196397	0.33 ± 0.09	-0.05	0.41 ± 0.05	0.03	0.36 ± 0.10	-0.02
HD 201237	0.10 ± 0.17	0.10	0.05 ± 0.07	0.05	0.07 ± 0.17	0.07
HD 209721	0.25 ± 0.12	-0.03	0.29 ± 0.04	0.01	0.26 ± 0.09	-0.02
HD 211706	0.09 ± 0.15	-0.00	0.09 ± 0.05	-0.00	0.10 ± 0.10	0.01
HD 218566	0.26 ± 0.09	-0.02	0.34 ± 0.08	0.06	0.24 ± 0.15	-0.04
HD 218750	0.14 ± 0.12	-0.03	0.23 ± 0.05	0.06	0.17 ± 0.09	-0.00
HD 221313	0.34 ± 0.13	0.03	0.31 ± 0.05	0.00	0.35 ± 0.11	0.04
HD 221974	0.40 ± 0.09	-0.06	0.47 ± 0.05	0.01	0.48 ± 0.10	0.02
HD 224383	-0.10 ± 0.13	0.00	-0.14 ± 0.04	-0.05	-0.02 ± 0.08	0.07
Intermediate population						
HD 8389	0.54 ± 0.10	-0.04	0.60 ± 0.05	0.02	0.57 ± 0.08	-0.01
HD 9174	0.36 ± 0.09	-0.05	0.50 ± 0.05	0.09	0.38 ± 0.10	-0.03
HD 12789	0.28 ± 0.05	0.01	0.31 ± 0.05	0.04	0.27 ± 0.08	0.00
HD 30295	0.33 ± 0.07	0.01	0.32 ± 0.04	0.00	0.30 ± 0.09	-0.02
HD 31452	0.19 ± 0.08	-0.04	0.23 ± 0.04	0.00	0.19 ± 0.09	-0.04
HD 37986	0.25 ± 0.04	-0.05	0.36 ± 0.04	0.06	0.27 ± 0.08	-0.03
HD 39715	-0.09 ± 0.11	0.01	-0.13 ± 0.06	-0.03	-0.14 ± 0.13	-0.04
HD 43848	0.35 ± 0.08	-0.08	0.40 ± 0.05	-0.03	0.37 ± 0.08	-0.06
HD 86065	0.03 ± 0.09	-0.06	0.11 ± 0.05	0.02	0.02 ± 0.10	-0.08
HD 87007	0.24 ± 0.09	-0.05	0.38 ± 0.05	0.09	0.23 ± 0.12	-0.06
HD 91585	0.23 ± 0.10	-0.02	0.29 ± 0.05	0.04	0.27 ± 0.10	0.02
HD 91669	0.41 ± 0.09	-0.03	0.48 ± 0.05	0.04	0.38 ± 0.12	-0.06
HD 182572	0.50 ± 0.05	0.02	0.46 ± 0.04	-0.02	0.50 ± 0.06	0.02
HD 196794	0.10 ± 0.07	0.04	0.04 ± 0.04	-0.03	0.08 ± 0.10	0.01
HD 197921	0.22 ± 0.11	0.00	0.24 ± 0.05	0.02	0.24 ± 0.10	0.02
HD 213996	0.34 ± 0.07	0.01	0.35 ± 0.05	0.02	0.35 ± 0.10	0.02
HD 214463	0.38 ± 0.11	0.04	0.32 ± 0.05	-0.02	0.32 ± 0.10	-0.02

**Appendix A: Online tables**

Table A.1: Log of spectroscopic observations.

star	$\alpha_{J2000}$ [h m s]	$\delta_{J2000}$ [d m s]	date	UT	exp [s]	Airmass	(S/N)
G 161-029	09:25:41.84	-06:46:05.80	2001 Jan 15	04:33:58	4500	1.15	57
BD-02 180	01:21:20.93	-01:43:45.62	2001 Jan 15	00:35:33	3600	1.54	64
BD-05 5798	22:20:19.62	-04:50:06.72	1999 Sep 27	04:54:58	2800	1.37	62
BD-17 6035	20:53:53.32	-16:45:54.98	1999 Sep 24	02:28:19	3600	1.14	65
CD-32 0327	00:15:14.75	-31:19:57.97	1999 Sep 26	06:50:42	3600	1.61	90
⋮	⋮	⋮	⋮	⋮	⋮	⋮	⋮

Table A.2: Data from the PASTEL catalogue.

Star	$T_{\text{eff}}$	$\log g$	[Fe/H]	Reference
HD 8389	5283 ± 64	4.37 ± 0.12	0.34 ± 0.05	Sousa et al. (2008)
	5378 ± 84	4.50 ± 0.12	0.47 ± 0.08	Sousa et al. (2006)
HD 9424	5420 ± 43	...	...	Masana et al. (2006)
HD 10576	5882 ± 56	...	...	Masana et al. (2006)
HD 13386	5226 ± 56	4.28 ± 0.09	0.26 ± 0.06	Sousa et al. (2006)
	5361 ± 43	...	...	Masana et al. (2006)
HD 15555	4820 ± 43	...	...	González Hernández & Bonifacio (2009)
	4855 ± 53	...	...	Ramírez & Meléndez (2005)
	4855 ± 67	...	...	Alonso et al. (1999)
⋮	⋮	⋮	⋮	⋮

Table A.3: Si, Ca, and Ti line list

Species	$\lambda$ (Å)	$\chi_{\text{exc}}$ (eV)	$\log gf$ (Sun)	$\log gf$ (BFL04)	$\log gf$ (NIST)	$\log gf$ (VALD)	$\log gf$ (BZO+09)
Si I	5665.56	4.92	-2.01	-1.94	-2.04	-1.75	...
Si I	5684.48	4.95	-1.63	-1.55	-1.42	-1.73	...
Si I	5690.43	4.93	-1.81	-1.77	-1.87	-1.77	...
Si I	5701.10	4.93	-2.00	-1.95	-2.05	-1.58	...
Si I	5708.40	4.95	-1.40	...	-1.47	-1.03	...
⋮	⋮	⋮	⋮	⋮	⋮	⋮	⋮

**Notes.** BFL04: Bensby et al. (2004); BZO+09: Barbuy et al. (2009).

Table A.4: Fe I and Fe II line list

Ion	$\lambda$ (Å)	$\chi_{\text{exc}}$ (eV)	C6	$\log gf$ (Sun)	$\log gf$ (VALD)	$\log gf$ (FW06)	$\log gf$ (MAGY09)
Fe I	5522.45	4.21	3.0200e-31	-1.49	-1.55	-1.52	...
Fe I	5546.51	4.37	3.9100e-31	-1.18	-1.31	-1.28	...
Fe I	5560.21	4.43	4.7900e-31	-1.14	-1.19	-1.16	...
Fe I	5577.02	5.03	1.0000e-32	-1.61	-1.55	...	...
Fe I	5618.63	4.21	2.9000e-31	-1.39	-1.28	-1.28	...
⋮	⋮	⋮	⋮	⋮	⋮	⋮	⋮

**Notes.** FW06: Fuhr & Wiese (2006); MAGY09: Meléndez et al. (2009); MB09: Meléndez & Barbuy (2009).